Aerospace Science and Technology 140 (2023) 108461

Contents lists available at ScienceDirect

Aerospace Science and Technology

journal homepage: www.elsevier.com/locate/aescte

Impact at aircraft level of elastic efficiency of a forward-swept tailplane

Salvatore Corcione [a,*], Vincenzo Cusati [b], Vittorio Memmolo [a], Fabrizio Nicolosi [a], Raul Llamas Sandin [c]

[a] Industrial Engineering Department of the University of Naples Federico II, Via Claudio 21, Naples, 80125, Italy
[b] Smartup Engineering, Piazza Salvatore Di Giacomo, 123, Naples, 80123, State Two, Italy
[c] Airbus Operations SL, Paseo John Lennon, Getafe, S/N 28906, State Two, Spain

ARTICLE INFO

Article history:
Received 21 December 2022
Received in revised form 26 May 2023
Accepted 14 June 2023
Available online 19 June 2023
Communicated by Christian Circi

Keywords:
Advanced rear end
Large passenger aircraft
Forward swept horizontal tailplane
Elastic efficiency

ABSTRACT

This paper evaluates the impact at aircraft level of the elastic efficiency of an advanced rear-end concept for a large passenger aircraft, exploiting a low-fidelity yet reliable aeroelastic approach. The innovative concept leverages a forward-swept horizontal tailplane to unlock a tail-fuselage connection such that a structural opening in the aircraft's rear-end is avoided. This installation allows for weight reduction in the structure, resulting in a positive impact on aircraft fuel burn. Moreover, a forward-swept tail has a different aerostructural behaviour that can be exploited to reduce its size with further weight and aerodynamic drag savings. In this respect, elastic efficiency is a crucial parameter for measuring the impact of this configuration at the aircraft design level. It takes into account both aerodynamic and structural characteristics, making it a comprehensive measure of effectiveness. Two different tail arrangements are being considered for an A320 neo-like aircraft: an innovative forward-swept design and a conventional layout that is equivalent. The results indicate that the forward-swept horizontal stabilizer has a higher elastic efficiency compared to the conventional tail arrangement. This could potentially lead to a reduction of the tailplane surface by approximately 2%, while still maintaining the same stability and control characteristics. This reduction in tail size unlocks the potential for fuel savings of approximately 0.5% on a mission profile of 3,400 nautical miles. Elastic efficiency is just one of the advantageous features of this innovative concept. By incorporating all the innovations proposed by the advanced rear-end concept, a weight reduction of up to 20% at the component level is expected. This could potentially result in fuel savings of approximately 2% for an aircraft similar to the A320neo, which has a mission range of 3,400 nautical miles.

1. Introduction

During the last few decades, the advancement of key enabling technologies has contributed to the improvement of transport aircraft in terms of aerodynamics, structures, propulsion systems, and more [1]. In recent years, numerous research studies have investigated possible novel aircraft configurations, proposing innovative layouts that significantly change the appearance of aircraft. One such example is the blended wing body design [2,3], box-wing or joined wings [4–6], double-bubble aircraft [7,8].

Despite the potential benefits that these innovative configurations introduce, they require drastic changes and add complexity, which can represent risky solutions for both manufacturers and airlines. To reduce the impact and risks associated with introducing complex solutions, a viable approach is to explore novel aircraft configurations that involve minor modifications to existing aircraft. In this respect, the Advanced Rear End concept (ARE) aligns with this idea.

Reductions in tail-plane size resulting from advancements in design and improvements in empennage efficiency and effectiveness have the potential to enhance aircraft performance by reducing fuel burn and weight. The penalties associated with meeting both longitudinal and directional stability and control requirements make up a significant portion of the total aircraft drag. Loads acting on aircraft tails contribute to the overall induced drag, compressibility, profile drag, structural weight, and maximum lift capability of the aircraft. The empennage of a typical Large Passenger Aircraft (LPA) accounts for one-fifth to one-fourth of the total lifting surface and 3% up to 6% of the maximum take-off weight. It contributes 5% to 8% to the total trimmed drag in cruise conditions [9].

* Corresponding author.
E-mail address: salvatore.corcione@unina.it (S. Corcione).

https://doi.org/10.1016/j.ast.2023.108461

Nomenclature

α_b	Percentage of absorption contribution of first spar
$x_{\bar{ac}_w}$	Wing aerodynamic centre position as fraction of mean aerodynamic chord
$x_{\bar{CG}_b}$	Maximum backward centre of gravity position as fraction of wing mean aerodynamic chordMaximum backward centre
$x_{\bar{CG}_f}$	Maximum forward centre of gravity position as fraction of wing mean aerodynamic chord
Δ_{rib}	Rib spacing
η_{flex}	Tail elastic efficiency parameter
Γ	Dihedral angle
Λ_{le}	Tailplane sweep angle at the leading edge
ν	Poisson modulus
AR_h	Tailplane Aspect Ratio
c_r	Root chord
c_t	Tip chord
c_{box}	Tail wing-box length (chord percentage)
$C_{L_{h,d}}$	Design lift coefficient for the horizontal tail
$C_{L_{MAX_{WB}}}$	Maximum lift coefficient of the wing-body configuration
C_{mac}	Wing mean aerodynamic chord
$d\epsilon/d\alpha$	Downwash gradient at horizontal tailplane
h_1	Height of the first spar of the tail wing-box (chord percentage)
h_2	Height of the second spar of the tail wing-box (chord percentage)
HTP	Conventional Horizontal Tail Plane
k_f	Rear end weight reduction coefficient
k_w	Fuselage rear end weight reduction coefficient
l_h	Longitudinal distance between wing-tail aerodynamic centres
L_{h_d}	Lift force at sizing condition for the horizontal tail
S_M	Safety margin
S_w	Wing reference area
s_y	Yielding stress
t_{rib}	Rib thickness
W_{MTO}	Aircraft maximum take-off weight
x_{ac}	Local tail section aerodynamic centre position (chord percentage)
x_{cg}	Local tail section centre of gravity position (chord percentage)
x_{ec}	Local tail section elastic centre position (chord percentage)
ARE	Advanced Rear End
b	Span
CFD	Computational Fluid Dynamics
E	Young modulus
EU	European Union
FEM	Finite Element Method
FSHT	Forward Swept Horizontal Tail
FSI	Fluid Structure Interaction
LPA	Large Passenger Aircraft
TR	Taper Ratio
VLM	Vortex Lattice Method
WB	Wing-Body configuration

The simplest unconventional solution is represented by the V-tail [10,11]. This solution is sometimes used in remotely piloted aircraft and has also been implemented in mass-produced manned aircraft, such as the Beechcraft Bonanza M35. However, the results of the NEFA [12] project concluded that while a V-tail configuration offered performance improvements due to its reduced wetted area, the added complexity and additional system resulted in no weight or cost benefits over a conventional empennage. A comprehensive study on advanced rear-end configurations was recently conducted in the EU-funded project NACRE [13] and demonstrated that such configurations could provide benefits in terms of reducing empennage drag, but not in terms of weight.

To further advance the introduction of rear-end concepts that effectively reduce drag and weight, this paper investigates the use of a forward-swept horizontal tailplane.

The adoption of a forward-swept tailplane enables a structural configuration in which the connection of the horizontal tail to the rear end does not necessitate a structural opening in a region of the fuselage that is heavily impacted by structural loads [14], as shown in the sketches of Fig. 1. By removing the structural opening at the rear end, the weight of the fuselage can be reduced by eliminating the need for local reinforcements to withstand aerodynamic loads. This solution also reduces fuselage deformation under aerodynamic loads, resulting in a more effective horizontal stabilizer surface [14].

Transonic aircraft wings typically have a positive sweepback. The main reason is linked to the aircraft encountering a vertical gust during its flight. In the case of positive sweepback, the bending deformation decreases the local angle of attack, resulting in a natural reduction of aerodynamic loads. In the case of a wing with a negative sweep angle, the effect is opposite. When encountering a vertical gust, the wing's bending causes higher local angles of attack, which increases loads and bending. As a result, static divergence may occur, leading to structural failure. Forward-swept wings are capable of withstanding significantly higher gust loads compared to wings with positive sweepback, which makes them heavier. Despite this drawback, some studies have investigated the possibility of exploiting the aerodynamic benefits of a forward-swept wing [15,16] proposing a solution to mitigate the coupling between flexional and torsional deformation by using aeroelastic tailoring techniques.

In terms of structural sizing, aeroelasticity is less demanding for wings with a relatively low aspect ratio. Thus, in the case of horizontal tails, introducing negative sweep angles could be a viable solution to improve the performance of the rear-end and empennage.

Forward-swept lifting surfaces offer several aerodynamic advantages over conventional sweepback designs. For a given leading edge sweep angle, forward-swept wings exhibit a shock-sweep angle that is five degrees higher than that of aft-swept wings [17]. Therefore, the implementation of a forward-swept design necessitates a smaller sweep angle at the leading edge in comparison to a positively swept-back layout with an equivalent sweep angle at the quarter chord line. A smaller sweep angle decreases the flow's inclination to move along the wingspan, leading to reduced aerodynamic drag. Moreover, in a forward-swept wing, the airflow moves from the tip to the root, resulting in higher stall angles [18], increasing the maximum aerodynamic forces or decreasing the tailplane area can result in the same maximum force while potentially reducing drag and weight.

The forward-swept design also offers another advantage due to its ability to deform elastically under aerodynamic loading. When a pure up-bending load is applied to an aft-swept wing, the different elastic displacements at the leading and trailing edges cause a decrease in the wing's incidence angles.

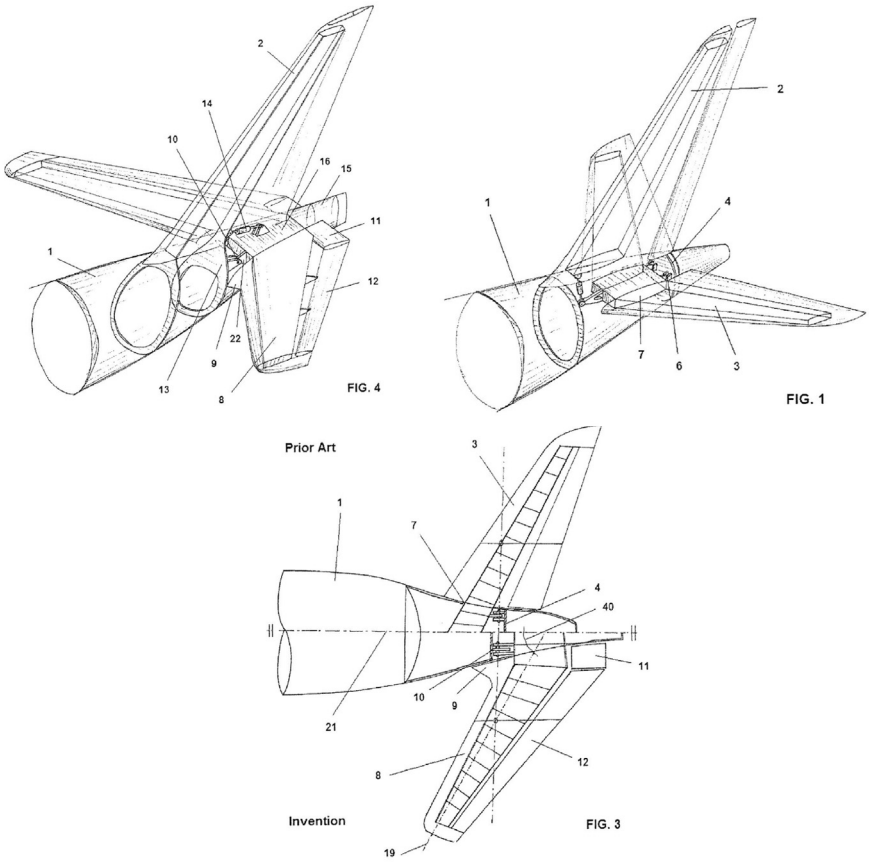

Fig. 1. Comparison between the structural arrangements of a conventional positive sweepback and a forward-swept tail [14].

This behaviour is reduced or even reversed when a forward-swept wing is considered, resulting in a higher aerodynamic lift gradient and improved stabilizing performance. With equivalent aerodynamic performance, reducing the size of the stabilizer can result in lower weight, cost, and drag.

To summarize, a forward-swept tailplane would be more efficient than a conventionally swept tailplane in terms of size, weight, and aerodynamic drag, provided that both stabilizer surfaces have their aerodynamic centre at the same distance from the wing's aerodynamic centre.

There is currently no publicly available research on the introduction of negative sweep angles on horizontal stabilizers. In general, there are few indications or applications that explore the effects of elastic efficiency on horizontal tailplane aerodynamics.

Obert in [19] illustrated the impact of elastic deformation on the longitudinal stability and control of a standard reference aircraft under varying dynamic pressures, collecting data from Skoog et al. [20,21].

To accurately estimate the elasticity of the tail, it is necessary to consider both aerodynamics and structural engineering. The current state-of-the-art approach for addressing aeroelastic problems involves conducting high-fidelity Computational Fluid Dynamics (CFD) and detailed Finite Element Method (FEM) analyses. The goal is to achieve the most accurate prediction of aerodynamic and structural interactions [22–24]. Furthermore, to attain a practical aircraft design and optimization, it is essential to consider multiple flight conditions and a significant number of design variables simultaneously, as demonstrated by Lyu and Martins [25,26]. Although several techniques, such as gradient-based methods or coupled adjoint [25,27] have the potential to reduce the number of function evaluations, implementing such an approach would result in a significant increase in computational cost, as demonstrated by Kenway and Martins in [27].

The benefit of using low-fidelity approaches is that they are relatively inexpensive, which makes it possible to gather larger amounts of data. However, one limitation of low-fidelity data is that it may not provide an accurate prediction of actual behaviour or fully encompass all of the physics involved in the problem being investigated.

Several efforts in developing and using reliable low-fidelity tools to solve aerostructural problems can be found in the literature.

Jasa et al. [28] demonstrated the development of coupled aerostructural software that utilizes low-fidelity tools to predict the aeroelastic behaviour of a wing. The software combines a Vortex Lattice Method (VLM) and 1-D finite-element analysis to model the lifting surfaces.

An improved approach is presented by Chauhan [29], where the lifting surface structure is modelled as a wing box consisting of upper and lower skins and two spars. This approach has been used to perform aerostructural optimization of the Boeing 777 wing with the goal of minimizing fuel burn. There was approximately 10% compliance with the results of the same optimization problem approached through high-fidelity tools by Brooks et al. [30] has been found.

A similar tool for aerostructural coupling is shown by Elham [31], where a method for optimization with lower computational cost is introduced. This tool calculates wing drag and structural deformation with accuracy comparable to higher fidelity CFD and FEM tools. An inviscid, incompressible vortex lattice method is combined with a viscous, compressible airfoil analysis code to predict drag on a three-dimensional wing in a quasi-three-dimensional aerodynamic solver. The wing's structural deformation

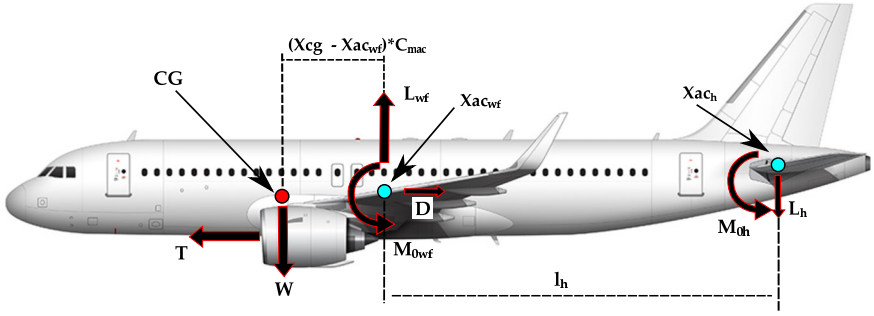

Fig. 2. Forces, moments, and lever arms are used to calculate the pitching moment of an aircraft.

and wing-box stress distribution are estimated using a finite beam element model.

FEM is not the only method for modelling the elastic behaviour of a wing, even when dealing with highly flexible lifting surfaces. A possible lightweight approach to addressing coupled aeroelastic problems involving large nonlinearities is presented by Changchuan [32,33]. These works employ a low-fidelity approach with the aim of reducing computational costs. To model large deformations of the wing, a non-planar vortex lattice method (VLM) is employed to predict aerodynamics, while a reduced-order model is used instead of an expensive non-linear finite element method (FEM) approach. The coupling between structures and aerodynamics is achieved through the use of the surface spline method. These models are computationally inexpensive compared to non-linear FEM, yet they still provide reliable results.

By utilizing a low-fidelity aerostructural approach, this paper aims to demonstrate how a single aspect of the proposed concept, namely elastic flexibility, can lead to a reduction in the size of the horizontal tailplane.

This paper aims to quantify the potential benefits of the advanced rear-end concept for large passenger aircraft. This represents a significant step forward in introducing the concept as a feasible solution for achieving significant fuel burn reduction and enhancing the performance of large passenger aircraft.

The rest of this paper is structured as follows. Section 2 briefly describes the preliminary sizing procedure for aircraft horizontal tails, defines the parameters under investigation, and outlines the methodology adopted for the aero-structural investigations. Section 3 reports the results dealing with two possible tailplanes geometry of a reference LPA aircraft similar to the Airbus A320-neo. The potential benefits in terms of fuel savings brought by the implementation of the proposed ARE concept are assessed in section 4. Finally, some conclusions and remarks are drawn in section 5.

2. Material and methods

This section provides a brief description of a commonly used approach for the preliminary sizing of a horizontal stabiliser. It also defines the elastic efficiency parameter and gives an overview of the methodology adopted to assess the aeroelastic calculations.

2.1. Elastic efficiency parameter and tailplane sizing

The horizontal stabilizer is typically designed to ensure a certain degree of static stability and provide sufficient control by achieving an appropriate maximum lift coefficient during downward lift. Critical factors that determine the size of the tailplane are typically the stability during cruise conditions and the control required for landing.

The effects of elastic deformation on tail aerodynamic behaviour are often overlooked during the preliminary sizing phase. However, when considering reducing the tail size to improve empennage aerodynamic efficiency and achieve aircraft performance gains through fuel burn and weight reduction, the elasticity of the tail may play a significant role.

The elastic behaviour of the tailplane affects both the stability and control of the aircraft. The common practice for determining the tail area during the preliminary sizing stage is to establish two relationships between the wing and tailplane area ratio, denoted as S_h/S_w, and the longitudinal distance between the centre of gravity and the aerodynamic centre, represented by $(X_{cg} - X_{ac_{wf}})/C_{mac}$. These relationships are used to satisfy the aforementioned sizing conditions. Referring to the force and moment diagram in Fig. 2, the elastic efficiency factor can be introduced.

This factor is defined as the ratio between the elastic and rigid lift curve slopes, as shown in Eq. (1), the sizing conditions can be expressed using Eq. (2) and Eq. (3).

$$\eta_{flex} = \frac{(C_{L_\alpha})_{elastic}}{(C_{L_\alpha})_{rigid}} \tag{1}$$

$$\frac{S_h}{S_w} = \frac{\left[C_{m_{0_{wf}}} + C_{m_{0_e}} + C_{L_{wf}}\left(X_{cg} - X_{ac_{wf}}\right)\right]C_{mac}}{\underbrace{\eta_{flex}}_{\text{elastic efficiency}} \quad \eta_h\left\{C_{L_h}\left[l_h + \left(X_{cg} - X_{ac_w}\right)C_{mac}\right] - C_{mac}C_{M_{0_h}}\right\}} \tag{2}$$

$$\frac{S_h}{S_w} = \frac{C_{L_{\alpha_{wf}}}\left(X_{cg} - X_{ac_{wf}}\right)}{\left\{\underbrace{\eta_{flex}}_{\text{elastic efficiency}} \quad \eta_h C_{L_{\alpha_h}}\left(1 - \frac{d\epsilon}{d\alpha}\right)\left[\left(X_{cg} - X_{ac_{wf}}\right) + \frac{l_h}{C_{mac}}\right]\right\}} \tag{3}$$

These equations are usually combined into a single graph, the so-called scissors plot [34], as shown by Fig. 3, where a qualitative scissors plot is illustrated. Between these limitations, for an assigned centre of gravity excursion range the minimum tail planform area can be estimated. The region of interest lies above the horizontal dashed line shown in Fig. 3. It is also worth highlighting that the aft centre of gravity is usually positioned at a safe distance from the natural stability limit which is, for a conventional jet transport aircraft, a value between 3% and 5% of the wing's mean aerodynamic chord [35–37].

By altering the effective lift curve slope of the horizontal tailplane, the elastic efficiency causes the stability and control limitation curves to exhibit a distinct slope from that of the rigid case. Generally, in a conventional positive sweepback arrangement, the tailplane area is oversized to compensate for the negative effects of elastic efficiency. In the case of a forward-swept tail, the two limitation curves may have a reduced slope, which allows for the possibility of reducing the minimum required tailplane area upon a specific centre of gravity excursion range.

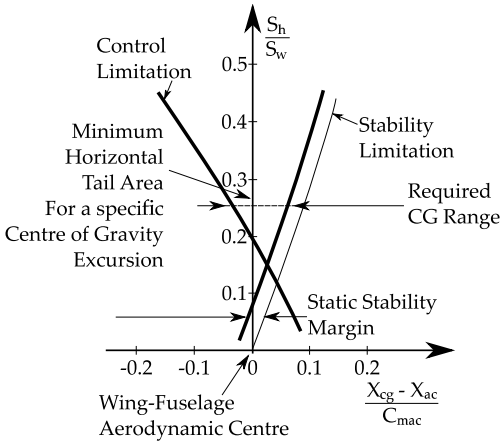

Fig. 3. A qualitative representation of the scissors plot diagram can be used to determine the minimum required horizontal tail area, taking into account control and stability limitations.

2.2. A low fidelity approach for fluid-structure interaction

The literature review clearly indicates that a low-fidelity approach can produce reliable results, even in cases where a lifting surface experiences significant elastic deformations.

It is worth highlighting that the applicability of the aforementioned approaches is limited to the extent that the elastic properties of a lifting surface are known.

To fulfil the aim of this research, a low-fidelity Fluid-Structure Interaction (FSI) approach has been developed. This approach relies on an enhanced VLM method for aerodynamic calculations and a semi-analytical approach for both structural sizing and deformation analysis. The two disciplines are interconnected, as shown by the conceptual workflow in Fig. 4.

The adoption of a low-fidelity approach is driven by the authors' ambition to conduct further research and explore a wide design space. The goal is to develop a prediction method, in the form of a surrogate model, for the elastic efficiency of aircraft tailplanes. This model can be used in the early stages of design.

The FSI process begins with generating an initial rigid tail shape using a set of macro design variables, which essentially refer to the planform parameters. The external rigid shape determines the masses and properties of key structural elements based on elasticity and stiffness, in accordance with specific structural layout and sizing conditions. Sizing conditions are determined based on the flight envelope diagram [38], including manoeuvring conditions, starting from a baseline aircraft.

Once the structural sizing has been completed, the shape of the tailplane is used to inform an enhanced vortex lattice method (VLM) developed by the research team of the authors [39] to calculate aerodynamic loads in specific conditions across various angles of attack, including nonlinear lift regimes.

Aerodynamic loads are transferred to the structural tool for each angle of attack to estimate the elastic deformation of the tail. The modified geometry, accounting for vertical displacements and sectional twists caused by torsion, is analyzed using the VLM code to update aerodynamic loads.

This data exchange is part of a converging loop that concludes when both the integral lift coefficient and the minimum squared error in the lift distribution between two consecutive iterations fall below a designated threshold. This loop is performed for both rigid and elastic tails across the assigned array of angles of attack.

More details about the used VLM method are provided in Appendix A.

Regarding the structural sizing and deformation analysis, an in-house developed tool has been adopted. This tool addresses the

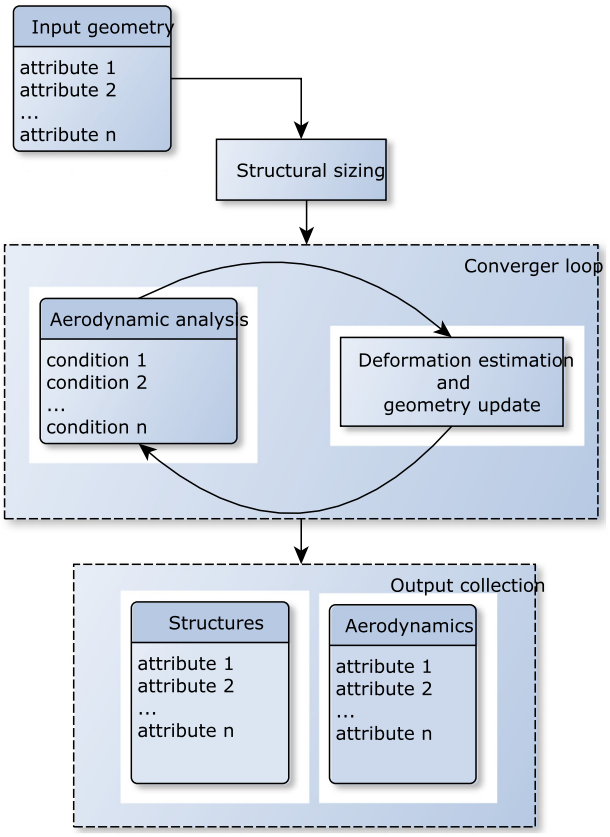

Fig. 4. Multidisciplinary aeroelastic workflow.

conceptual definition of a lifting surface and facilitates the preliminary sizing of its structural components.

To determine the critical loading condition on the tail and drive the structural sizing, the first step is to construct the classical V-n diagram for the aircraft in question. According to the aircraft category examined in this paper, the FAR25 regulation [40] can be utilized to establish the flight envelope and then estimated the balancing loads required to the tailplane, including the most critical manoeuvring conditions.

The tailplane is modelled as a combination of primary and secondary structures. The mass of the primary structure is calculated using basic structural analysis that relies on estimates of stress and deformation. The distribution of internal stresses acting on the lifting surface is derived using a beam-like approach, taking into account the contributions of various bearing elements. The optimal size of the wing is achieved by considering the weight of spar caps, webs, ribs, stringers, and panels in the wing box to obtain the minimum overall weight of the wing. Moreover, the computation of the primary structure mass takes into account bending moment relief, material properties, weight penalties and the bending-twist coupling to correctly estimate the load condition of a swept planform.

Regarding load absorption, the spar caps are primarily responsible for resisting bending and can withstand the in-plane stress that results from it. The spar webs are sized to withstand the shear forces that act on the section, as well as the external forces that are perpendicular to the surface of the wing box, and the torsion that is induced by aerodynamics. The latter also provides the basis for establishing the thickness of the skin. This is clearly a rough assumption that is neither overly cautious nor unsafe. Actually, since each component bears its own load, the combined action can alter the local stress field and lead to suboptimal component sizing. However, despite some localized effects, these assumptions are

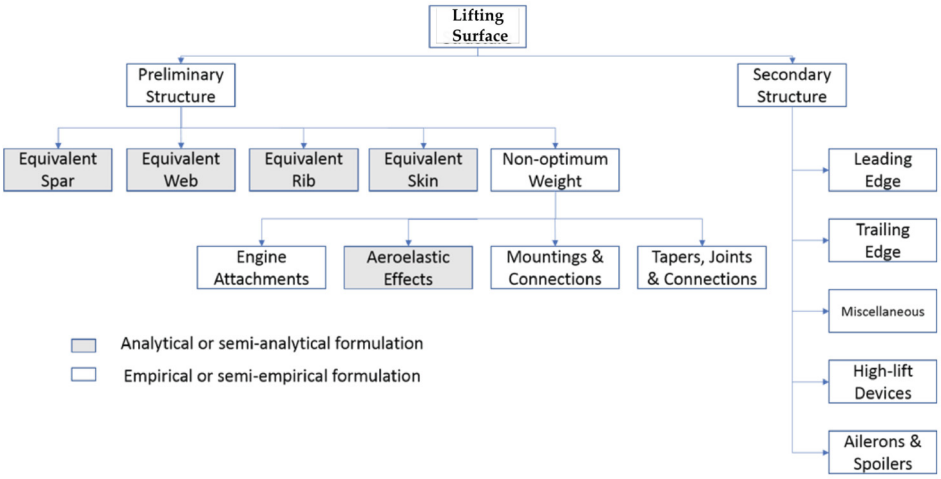

Fig. 5. Lifting surface structural decomposition.

well-suited for the preliminary sizing of aerostructures. In addition, a property constraint is included to address manufacturing issues, and a minimum thickness and/or area is always maintained for each component. The procedure returns the distribution of properties for each element in terms of mass and geometry. The former provides the total mass of the tailplane when integrated across the entire wingspan. The latter allows for the estimation of the structural stiffness across the wingspan. Specifically, EI(y) provides the distribution of bending stiffness along the wingspan, while GJ(y) provides the distribution of torsional stiffness.

The amount of mass required is only enough to withstand critical loads and-or deformation. The secondary structure is composed of fixed leading and trailing edges, control surfaces, and high-lift devices. The weight of these components is estimated using statistical methods that depend on their geometry [41]. As described above, the problem of tail mass can be expressed as the sum of primary and secondary structure masses. An outline of the structural classification of several components is reported in Fig. 5.

Complex structural phenomena, such as effects of combined loads, dynamic effects and so on, are neglected. Distortion of cross-section is not considered, flat sections remain flat after load application.

More details about the proposed structural approach are provided in Appendix B

3. Case studies: conventional and forward-swept horizontal tailplanes

The software chain described in section 2, allows to perform low-medium numerical investigation on several geometries in a relatively short amount of time.

Two reference geometries were selected to measure the potential benefits, if any, of the FSHT in terms of weight, elasticity, and aerodynamics.

The reference geometries were provided by Airbus as part of the European project IMPACT [42].

As stated above, it was expected that the elastic tailplane behaviour would improve under aerodynamic loads due to the negative sweep angle. This configuration should withstand bending and torsion loads differently than the conventional configuration with a positive sweep angle value. Indeed, the angular deformation results in a higher effective angle of attack of the tailplane, which in turn increases its lift capability. The main geometric parameters are shown in Fig. 6, and collected in Table 1 and Table 2.

Following the procedure described in the previous section, it was possible to accurately size the tailplane structure according to

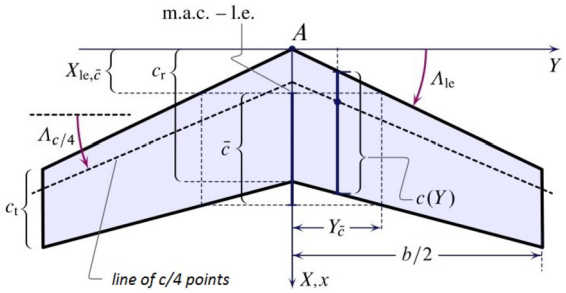

Fig. 6. Sketch of tailplane geometry with a description of the main parameters.

Table 1
Geometric data of a conventional configuration.

Symbol	Value	Unit	Description
b	12.45	m	tail span
c_r	3.74	m	root chord
c_t	1.36	m	tip chord
Λ_{le}	32.30	deg	sweep angle at l.e.
Γ	6.00	deg	dihedral angle
TR	0.331		taper ratio
S_h	30.99	m^2	tail surface
AR_h	5.00		aspect ratio

Table 2
Geometric data for FSHT configuration.

Symbol	Value	Unit	Description
b	12.45	m	tail span
c_r	2.72	m	root chord
c_t	1.90	m	tip chord
Λ_{le}	-15.00	deg	sweep angle at l.e.
Γ	0.00	deg	dihedral angle
TR	0.700		taper ratio
S_h	30.99	m^2	tail surface
AR_h	5.80		aspect ratio

the specific load scenario derived from the representative manoeuvring envelope for the primary structure. Table 3 presents data for the wing-fuselage configuration. Sizing loads are collected in Table 4, Table 5 illustrates the material, and Table 6 reports the wing box characteristics.

The distribution of bending and torsional stiffness for both conventional and forward-swept tails is shown in Fig. 7 and in Fig. 8. The weight for both tailplane geometries is shown in Table 7. Once the weight and stiffness distributions have been assessed, the aeroelastic cycle is performed for each of the two configura-

Table 3
Main aircraft characteristics.

Symbol	Value	Unit	Description
S_w	125.0	m^2	wing surface
C_{mac}	4.29	m	wing m.a.c.
l_h	17.19	m	wing-tailplane a.c. distance
$C_{L_{max_{WB}}}$	1.377		WB maximum lift coefficient
$x_{\vec{ac}_w}$	0.25		position of the wing a.c.
W_{MTO}	724.9	kN	Maximum Take Off weight
$\bar{x}_{CG_f}$	0.17		maximum forward position of CG (% of wing C_{mac})
$\bar{x}_{CG_b}$	0.37		maximum backward position of CG (% of wing C_{mac})

Table 4
Sizing load results.

Symbol	Value	Unit	Description
L_{h_d}	-28.9	kN	design horizontal tail lift force[a]
$C_{L_{h,d}}$	-0.11		design horizontal tail lift coefficient (conventional)
$C_{L_{h,d}}$	-0.11		design horizontal tail lift coefficient (FSHT)

[a] estimated as suggested by Calcara [43], based on FAR 25.331

Table 5
Characteristics of the material.

Symbol	Value	Unit	Description
ρ	1500	kg/m^3	Density
s_y	200	*MPa*	Yielding stress
E	84	*GPa*	Young modulus
G	14.5	*GPa*	Shear modulus
ν	0.35		Poisson modulus
S_M	2.0		Safety margin

Table 6
Characteristics of the wing box.

Symbol	Value	Unit	Description
h_1	0.14		height of first spar (chord percentage)
h_2	0.08		height of second spar (chord percentage)
α_b	0.70		percentage of absorption contribution of first spar
c_{box}	0.45		wing box length (chord percentage)
t_{rib}	2.00	mm	rib thickness
Δ_{rib}	0.50	m	rib spacing
x_{ac}	25%		aerodynamic centre position (chord percentage)
x_{cg}	35%		centre of gravity position (chord percentage)
x_{ec}	40%		elastic centre position (chord percentage)

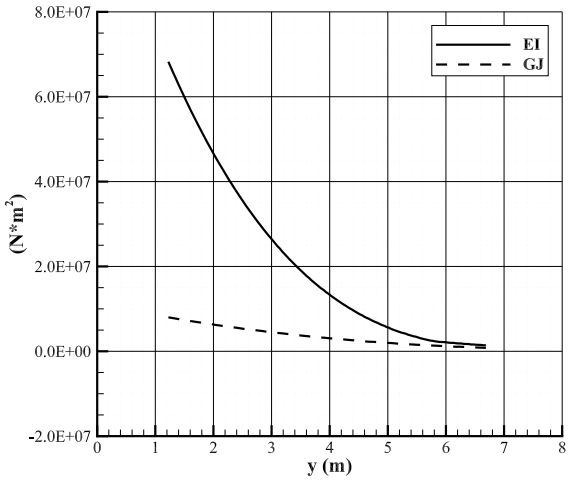

Fig. 7. Bending and torsional stiffness distribution for the conventional tailplane (exposed) using a semi-analytical method.

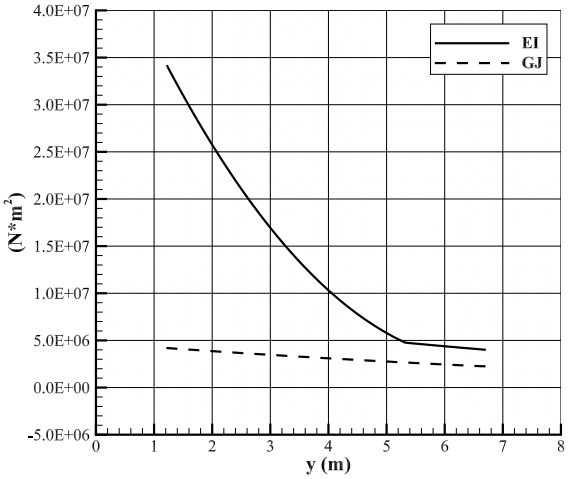

Fig. 8. Bending and torsional stiffness distribution for the exposed tailplane of the FSHT using a semi-analytical method.

Table 7
Mass comparison between the two cases.

	Conventional	FSHT	Δ
Mass (kg)	569.3	566.5	-0.5%

Table 8
Flight conditions for aeroelastic analysis.

	Altitude	Mach number
High-speed condition	11 000 m	0.78
Low-speed condition	sea level	0.2

tions. The flight conditions are listed in Table 8. The procedure begins with estimating the aerodynamic load for the rigid tailplane configuration using an aerodynamic tool to determine the spanwise lift distribution, denoted as $C_l(y)$. The distribution of weight, torque from pitching, and other forces exerted on the structure cause stress, resulting in a specific strain that includes a distribution of twist angles. This strain serves as the input for the second step of the cycle. It was necessary to interpolate data on the same query points in order to provide useful input for the aerodynamic tools. This was done by starting with the output of the structural analysis. During the second step of the cycle, a new distribution of twist angle resulting from aerodynamic loads (and weight) was applied to the structure that had been deformed in the previous step. The cycle ends when the difference between the twist distributions of the two steps is below a certain threshold. Since the objective was to estimate the ratio between the slope of the *rigid* and elastic lift coefficient curves, it was necessary to perform the aeroelastic cycle at different angles of attack. In this case, the cycle was performed at three angles of attack: -4, -2, and 0 degrees.

Table 9
Estimated value of η_{flex}.

	Conventional	FSHT
η_{flex} *@high-speed condition*	0.95	1.00
η_{flex} *@low-speed condition*	0.98	1.00

As mentioned earlier, the two tailplanes exhibit a distribution of torque moment with opposite signs because of their sweep angle. In particular, the torsion of the forward-swept tailplane is influenced by a deformation denoted by $\theta(y)$, which amplifies the magnitude of the angle of attack. This results in a more negative angle than the rigid case would produce. Conversely, the conventional tailplane experiences a decrease in the lift gradient when compared to the forward-swept tailplane. The positive effect of torsion can be measured by the η_{flex} parameter. This parameter is defined as the ratio between the rigid and elastic values of the lift coefficient curve slope ($C_{L_{\alpha h}}$), as shown in Eq. (1).

The majority of the effort put into this research could probably be summarized by the results reported in Table 9. The back-swept geometry is characterized by a reduction in the lift gradient ($\eta_{flex} < 1$) at high-speed conditions, whereas the forward-swept tailplane maintains an almost constant lift coefficient curve slope ($\eta_{flex} \approx 1$). However, the impact of flexibility is significantly diminished by the decrease in dynamic pressure, as the η_{flex} value for low-speed conditions is approximately 0.98.

Indeed, one of the main objectives of this work was to determine how to incorporate higher elastic efficiency into the design process for the FSHT configuration. It is crucial to identify the tail with the lowest area that complies with both the linear and non-linear design criteria at the same time [14].

The values of flexibility indices in Table 9 suggest that it is possible to reduce the surface area of the forward-swept tailplane by approximately 5%, resulting in several beneficial consequences such as weight and drag reduction. This reduction in weight and drag leads to a block fuel reduction, which creates a positive snowball effect. This is due to the favourable elastic behaviour of the tailplane.

However, despite implementing the scissors plot approach described in section 2, the potential surface reduction was limited by the minimal impact of flexibility during low-speed conditions (approximately 2%). Nevertheless, it is important to remember that the so-called non-linear capabilities are also crucial for designing the tailplane, as clearly explained in [14]. In this respect, the tailplane is usually designed with great consideration given to the maximum (negative) lift coefficient, which is a fundamental parameter for handling quality as mentioned in Section 1. A realistic prediction of these parameters can only be achieved with high-fidelity tools such as a CFD-RANS solver. So far as the output of the aeroelastic analysis is concerned, the possible surface reduction should be considered equal to 2% (applying linearly the structural gain due to elasticity).

3.1. Benchmarking: FEM and CFD

This section presents the results of a validation test comparing the low-fidelity approach to high-fidelity aerodynamic and structural analyses for the proposed forward-swept tailplane. To emphasize the importance of the validation phase, the analysis is conducted under critical sizing conditions for the tailplane structure.

3.1.1. FEM analysis

To validate the airframe design for the advanced rear-end, the structural parameters are detailed, and a high-fidelity framework for structural analysis is established. The process explained here aims to estimate the deformation of the initial structural design, including the spar, web, rib, and skin, all of which are components of the low-fidelity model.

The preliminary Finite Element (FE) model obtained from the mass estimation process described in the previous section is shown in Fig. 9 (a). The global horizontal tailplane finite element model consists of linear shell and beam elements for various airframe components. The spar and rib webs, as well as the horizontal tail skins, are modelled as shell elements, while the spar and rib caps and stringers are modelled as beam elements. The load cases used for design and mass estimation are also utilized for a more comprehensive structural strength assessment.

In particular, the configuration shown in Fig. 9 (b) is the FE idealization of the FSHT design carried out for the increased fidelity structural assessment.

The internal layout consists of a wing box structure with 12 bays, 10 stringers, and 12 skin panels per bay (6 for the upper and 6 for the lower skin), whose properties are equivalent to those of the semi-analytical model.

However, the elements of the same bay are not tapered, i.e. the thickness of the shell and the area of the stringer keeps constant all through the bay and steps at the rib web. The box is then closed with leading and trailing edges through shell elements too. The static linear analysis is carried out by running SOL101 in NX Nastran.

The comparison of the spanwise distribution of the vertical displacement and the twist angle around 40% chord is shown in Fig. 10 (a) and (b), respectively. In both cases, a slight difference can be caught close to the root and the tip of the tail. Otherwise, there is excellent agreement between low-fidelity and high-fidelity solutions. The misalignment is due to the nonlinear effects of the boundaries (root) and the lack of taper along the bay (tip). In both cases, the finite element model is slightly stiffer than the semi-analytical model. However, the effect on the global scale is quite negligible.

3.1.2. Aerodynamics

The reliability of the aerodynamic loads predicted using the enhanced VLM approach has been validated through a high-fidelity CFD analysis. The reliability and accuracy of the VLM are benchmarked by comparing the lift coefficient distribution, the global lift coefficient, and the angle of attack required to generate the ultimate downforce as prescribed by the structural sizing process.

The geometry of the tailplane is described by the planform parameters listed in Table 2, the sizing downforce is approximately 30 tons, as illustrated in Table 4, and corresponds to a tail lift coefficient of -0.11. The high-fidelity analysis was performed using the commercial software STARCCM+ [44]. The numerical model setup details are reported in Table 10, whereas Fig. 11 shows a comprehensive view of a typical fluid domain and the application of boundary conditions.

The variables, mesh, and scheme used for the VLM are illustrated in Fig. 12. The VLM approach, used as a linear solver for the enhanced-nonlinear VLM, divides the tailplane surface into multiple spanwise panels. A single horseshoe vortex is placed in each panel at 1/4 of the local chord, and its free-stream sections extend to infinity. Control points are placed at 3/4 of the chord length, where the unit normal vector is computed. The number of sections used as input for the VLM span is 8, while the aerodynamic data is computed by dividing the lifting surface into 50 cross-sections.

The comparison of the spanwise distribution of the lift coefficient is shown in Fig. 13. In the case of a rigid structure, there is excellent agreement between low-fidelity and high-fidelity solutions. Table 11 presents the results of the validation case, which compares the total lift coefficient of the tailplane and the corre-

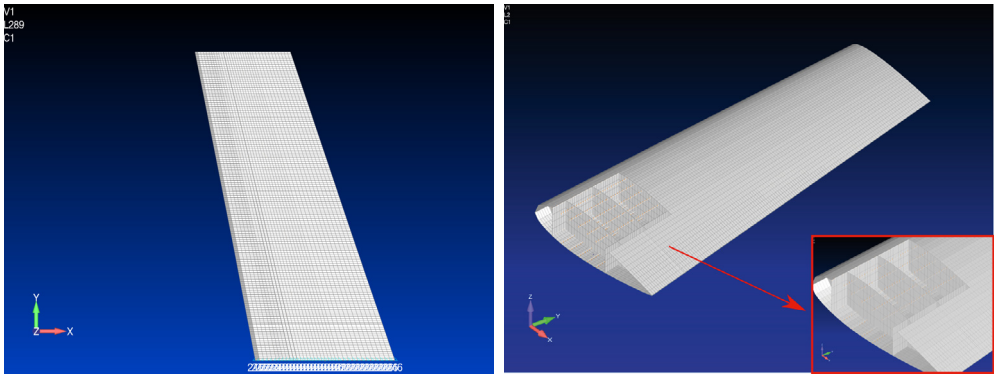

Fig. 9. Top (a) and isometric (b) views of the finite element model of the FSHT.

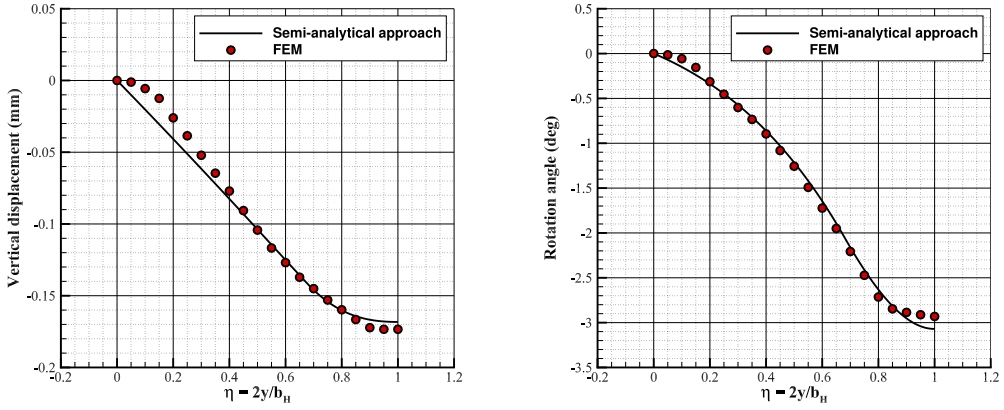

Fig. 10. Vertical displacement and twist angle: FEM vs. Semi-Analytical Approach.

Table 10
Numerical setup and mesh characteristics for high-fidelity CFD analysis.

Parameter	Value
Domain span	16 $b_H/2$
Domain height	30 $b_H/2$
Domain length	100 $b_H/2$
Mesh type	unstructured polyhedral
On body minimum surface size	0.0042 (m)
On body target surface size	0.035 (m)
Number of volume cells	11 183 156
Number of prism layers	25
First cell wall distance	$1e^{-6}$ (m)
Turbulence model	SST $\kappa - \omega$
Flow model	Compressible
Inflow boundary condition	Free stream
Outflow boundary condition	Pressure outlet
Number of iterations	5000
Mach number	0.2
Flight altitude	sea level

Table 11
Rigid aerodynamic results: CFD vs. VLM.

	VLM	CFD
Lift coefficient	-0.12 (w.r.t. S_W) -0.47 (w.r.t. S_H)	-0.11 (w.r.t. S_W) -0.46 (w.r.t. S_H)
Angle of attack	-4.61 deg.	-4.66 deg.

sponding angle of attack achieved. These global parameters are analyzed to assess the accuracy of the simulation.

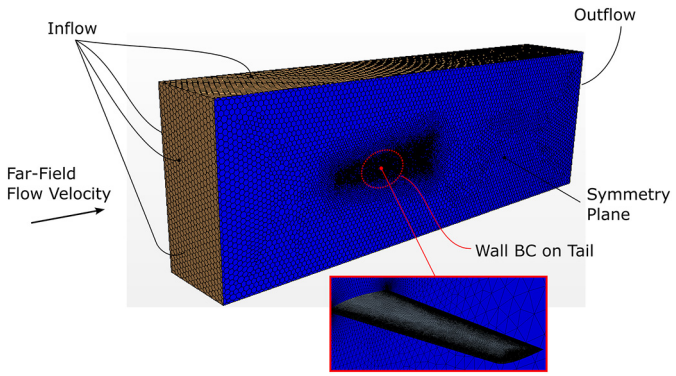

Fig. 11. Fluid domain and boundary conditions using STAR-CCM+.

Further demonstration of the proposed method's reliability is the comparison of spanwise lift coefficient distributions under elastic deformation. As can be seen in the chart in Fig. 14, the overall lift distribution is not affected by the slight differences between the vertical displacements and rotation angles calculated through the semi-analytical or FEM approach (see Fig. 10).

The final benchmark involves comparing the aerodynamic load estimated by both the VLM and CFD approaches on the elastic forward-swept tail, taking into account the deformation calculated through the FEM tool. This comparison is shown in Fig. 15 highlights the accuracy of the enhanced VLM tool in predicting loads, even in the case of an elastically deformed lifting surface.

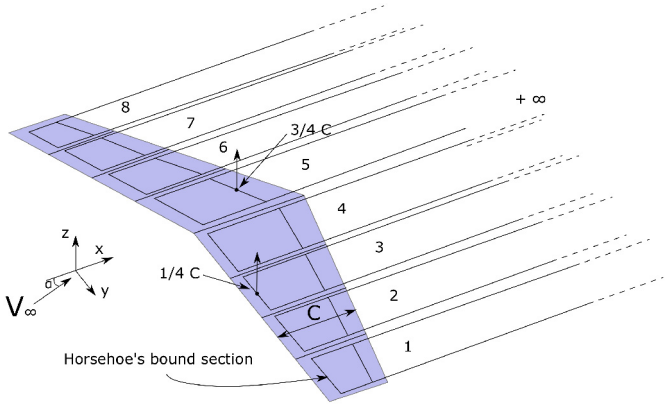

Fig. 12. System of horseshoe vortices, mesh, and variables in the VLM solver.

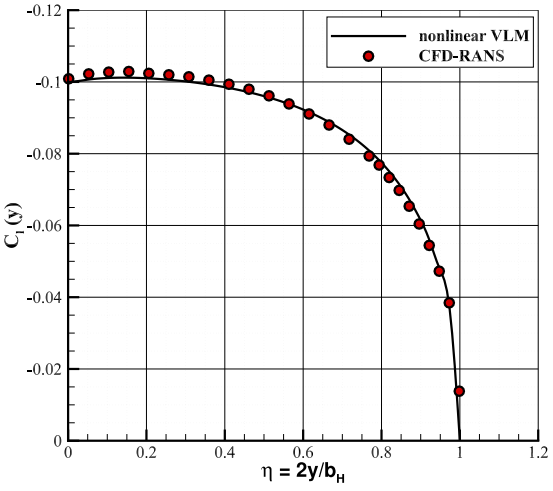

Fig. 13. Lift coefficient distribution for the rigid case: VLM vs CFD.

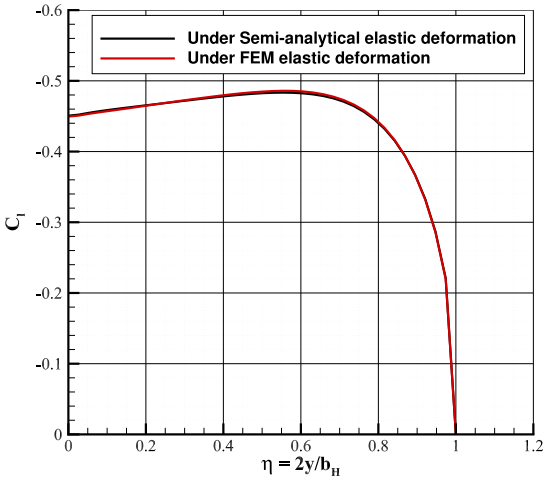

Fig. 14. The effects of deformations, calculated using both FEM and semi-analytical approaches, on the lift coefficient distribution estimated through the VLM.

4. Impact at aircraft level

According to the scissors plot approach, the elastic efficiency of the forward-swept tail suggests a potential reduction of the minimum tail area of about 2% (for a fixed range of centre of gravity excursion).

This section will address the potential impact of reducing the tail area on the aircraft using a multidisciplinary tool [45,46].

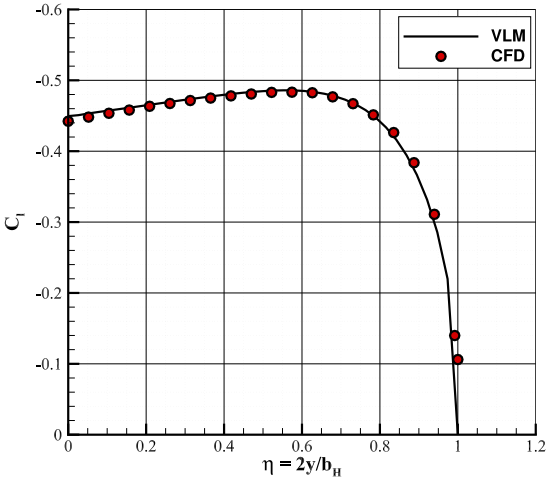

Fig. 15. The comparison between the lift distribution of the elastic forward-swept tail estimated through the VLM and CFD tools.

The reference for a large passenger aircraft is a platform similar to the A320neo. The three views are shown in Fig. 16, whereas some of the main overall aircraft data are presented in Table 3. A design mission profile of 3,400 nm has been considered for a 180 seats capacity. An overview of the considered design mission profile and flight performance of the reference aircraft is shown in the infographic of Fig. 17.

Through a multidisciplinary analysis, it is possible to evaluate the impact of a potential reduction in tailplane area on the aircraft's maximum takeoff weight and fuel burn.

To conduct a fair comparison between the conventional and advanced rear-end designs, the forward-swept tailplane is slightly shifted back to maintain a constant tail-level arm. This is accomplished by keeping the tail aerodynamic centre in the same position as the conventional tailplane arrangement while adhering to the trim axis constraint. This is illustrated in Fig. 18.

The key results of the multidisciplinary analysis on the design mission of 3,400 nm, are presented in Table 12.

Most of the load on the tailplane is due to the lift acting on the fuselage at pivot points that define the hinge line. The trimming actuator provides an additional reaction to the pitching moment. In the conventional arrangement, the pivot points are positioned behind a significant structural cut-out. This cut-out is necessary to enable the adjustment of the tailplane incidence angle, which is used to trim the aircraft during various flight conditions. Significant structural reinforcements are required to provide sufficient strength to the rear fuselage in this area. Shear deformations may have a non-negligible effect on the elastic efficiency of the tailplane. In the FSHT layout, the aerodynamic load acts directly on a closed section of the fuselage because the cut-out is located aft of the pivot points, in a lightly-loaded section. The weight savings resulting from different arrangements could be directly correlated to the wet area of the rear fuselage, which has been assumed to be constant.

Assuming identical cabin geometry from the aircraft's centre of gravity to the rear pressure bulkhead in both configurations, the pressurized section of the fuselage will experience the same bending moment distribution (excluding second-order effects of dynamic loads). This should lead to an equivalent weight of the fuselage's pressurized section. The rationale for this assumption is based on the fact that, given a specific trim condition provided by the empennage, the pitching moment around the aircraft's centre of gravity is the crucial characteristic that must be achieved. At its origin, this global pitching moment is produced by the lift generated by the tailplane. This lift can be assumed to act on the hinge

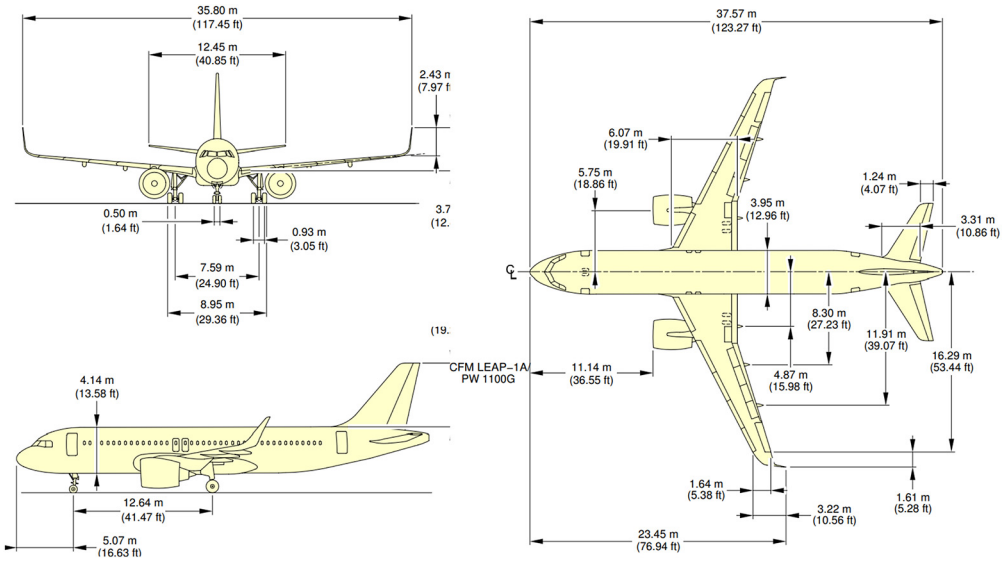

Fig. 16. A320 neo three views.

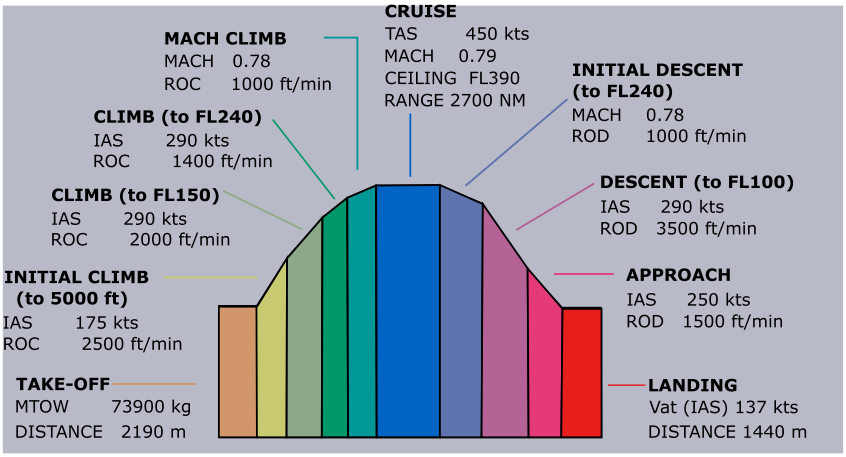

Fig. 17. Graphical abstract of A320 neo like aircraft mission profile and performance.

Table 12
Impact of the tailplane area reduction at aircraft level.

	Conventional	FSHT -2% S_h
W_{MTO}	73,900 kg	73,781 kg
Total Fuel and Reserve	17,300 kg	17,207 g
Block Fuel	15,400 kg	15,378 kg
Horizontal tail mass	569.3 kg	555.10 kg
Wing mass	7,760 kg	7,757 kg
Fuselage mass	7,120 kg	7,120 kg
Take-Off Field Length	2,190 m	2,200 m
Landing Field Length	1,440 m	1,440 m

line, whose location remains fixed. Therefore, it seems reasonable to assume that the weight of the pressurized section of the fuselage is not affected by the empennage design as long as it provides the required moments. Additionally, the local effects around the tailplane attachment are expected to be of relatively minor importance.

As can be seen from the results in Table 12, the implementation of this innovative tail arrangement has the potential to reduce weight by approximately 0.2%. The latter results in a fuel saving of only about −0.51% of the total fuel required for the design mission of 3,400 nm, while the block fuel remains unchanged.

It must be remarked that the higher elastic efficiency of the forward-swept tail is only one of the innovative features of the

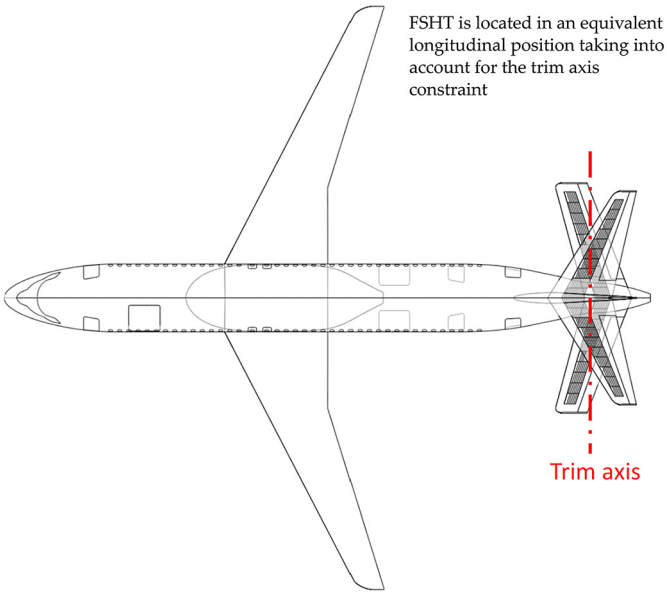

Fig. 18. Longitudinal trim axis constraint for the location of FSHT.

Table 13
Impact of potential rear-end weight reduction.

	HTP	$k_f = 0.90$	$k_f = 0.85$	$k_f = 0.80$
W_{MTO}	73,900 kg	73,263 kg	72,603 kg	71,944 kg
Total Fuel and Reserve	17,300 kg	17,165 kg	17,046 kg	16,927 kg
Block Fuel	15,400 kg	15,334 kg	15,228 kg	15,123 kg
Horizontal tail mass	569.3 kg	555.1 kg	555.1 kg	555.1 kg
Wing mass	7,760 kg	7,717 kg	7,671 kg	7,625 kg
Fuselage mass	7,120 kg	6,780 kg	6,403 kg	6,027 kg
Take-Off Field Length	2,190 m	2,157 m	2,114 m	2,072 m
Landing Field Length	1,440 m	1,421 m	1,413 m	1,406 m
Cruise Mach number	0.79	0.79	0.79	0.79
Static Stability Margin*	$\simeq$ 5.00%	$\simeq$ 5.00%	$\simeq$ 5.00%	$\simeq$ 5.00%

*$@X_{cg}/C_{mac} = 0.37$

proposed Advanced Rear End. The key aspect of the proposed concept is the ability to eliminate the fuselage cut-out, which eliminates the need for local reinforcements to withstand the bending and torsional loads introduced by the horizontal and vertical tail. Loads coming into the aircraft from the empennage are transferred through special highly loaded frames. Conventionally, these are always manufactured in metal. However, in the Advanced Rear End project, they are made using composite materials. The highly loaded frames in the composite material are likely the most significant technological component, aside from the radical configuration itself, in the Advanced Rear End project. By combining these technologies with a new rear-end design configuration, weight savings of up to 20% can be achieved compared to the rear end of a traditional single-aisle aircraft [47].

Within the framework of European project IMPACT [42], the assessment of the fuselage and forward-swept tail aerostructure design and optimisation in the Advanced Rear End concept is still progressing through high fidelity tools for both the aerodynamics and structural disciplines. To provide a preliminary estimate of the impact at aircraft level coming from the expected weight savings, a parametric investigation is here presented. The parametric investigation is accomplished by simply assuming a scaling factor to be applied to the rear end. An array of fuselage rear-end weight reduction factor k_f of -10%, -15% and -20% has been assumed. To combine the tail elastic efficiency behaviour with the potential fuselage rear-end weight reduction, the reference horizontal empennage will be the FSHT with a reduced planform area.

Results of this parametric investigation are summarized in Table 13.

According to the results of the parametric investigation, if the Advanced Rear End technology could reduce the weight of the rear end components by 20%, it would result in a potential saving of up to 3% of the maximum take-off weight. This translates to a fuel saving of approximately 2% (based on a design range of 3,400 nm) compared to a traditional single-aisle aircraft. This result is in line with Clean Sky's environmental objectives [47].

5. Conclusions

This paper evaluated the prediction of elastic efficiency in horizontal tail planes using a reliable, low-fidelity, and lightweight approach. The study also evaluated the potential advantages of various elastic behaviours in an innovative rear-end design. The research focuses on optimizing the aero structure of large passenger aircraft, with a particular emphasis on an advanced rear-end design that incorporates a horizontal tail featuring a negative sweepback. The investigated concept aimed to decrease the size of the tail and enhance the efficiency of the empennage, potentially leading to better aircraft performance through reduced fuel burn and weight at the rear end. The main focus of this paper is to predict the efficiency of tail elasticity, which is defined as the ratio between the lift curve slope of the elastic and rigid configurations.

The aeroelastic analysis revealed that the innovative forward-swept horizontal stabilizer has the potential for weight reduction compared to the conventional configuration, providing advantages. The weight savings derived from the forward-swept tailplane's ability to balance the aircraft throughout its flight envelope and provide the same handling quality as a conventional tailplane, but with a reduced planform area. These capabilities refer to the so-called "linear" criteria used in the design of a horizontal tailplane. The primary parameter used is the lift gradient of the tailplane. A software tool has been developed to quantify the potential benefits of elasticity for innovative design. This is accomplished by defining a new efficiency index as the ratio between the lift gradient of the rigid and elastic tailplanes, for both conventional and forward-swept configurations. The results revealed that the conventional configuration experienced a reduction of the lift gradient by 5%, whereas for the innovative configuration, the lift gradient remained practically the same as the rigid case.

A reduction of approximately 5% in the horizontal surface area could be achieved by linearly applying the elasticity benefit of the structure, if only the high-speed condition (cruise) is taken into consideration during the empennage sizing process. However, it is also essential to confirm the low-speed condition to guarantee adequate control of the aircraft during the takeoff and landing phases. In low-speed conditions, characterized by low dynamic pressure, the low-fidelity methodology discussed in this paper indicates that reducing the area of the horizontal tailplane would result in a potential reduction of only 2%.

Once the assessment of the elastic efficiency factor is complete, the potential benefits in terms of weight reduction and fuel savings can be evaluated at the aircraft level. This can be achieved by utilizing a multidisciplinary tool to conduct a simulation-based mission analysis.

The results of this investigation showed a potential weight reduction and, consequently, a fuel saving of less than 1%.

This highlights that elastic efficiency is not the only distinctive feature of the proposed Advanced Rear End concept that can be utilized to achieve significant reductions in structural mass and fuel consumption.

The key features of the investigated ARE concept are related to the ability to eliminate the fuselage cut-out and transition to a fully composite rear end, which could potentially reduce structural mass by up to 20%. The estimated impact of reducing weight on A320neo-like aircraft shows a potential fuel saving of approximately 2% on a design mission of 3,400 nautical miles.

However, from a broader perspective, the design of the horizontal tailplane is not solely driven by structural considerations. As part of the IMPACT project, the suggested rear-end configuration is undergoing a thorough process of aerodynamic design and optimization. The design of the tail is constrained not only by linear factors but also by non-linear factors, such as handling quality. The maximum (negative) lift coefficient of the tailplane is a critical parameter in determining the quality of handling. From this

perspective, the optimization of aerodynamics is driving the development of unique aerodynamic features in the forward-swept tail, resulting in a reduction of the tailplane area. This is achieved by utilizing passive leading edge extension devices. The latter should lead to further reductions in the size of the horizontal tail or a shorter rear-end while maintaining the same level of stability, control, and handling quality of the aircraft.

6. Authors contribution

Conceptualization: Salvatore Corcione, Vincenzo Cusati and Vittorio Memmolo.
Methodology: Salvatore Corcione, Vincenzo Cusati, and Vittorio Memmolo.
Software: Salvatore Corcione, Vincenzo Cusati, and Vittorio Memmolo.
Validation: Salvatore Corcione, Vincenzo Cusati, Vittorio Memmolo and Raul Llamas Sandin.
Formal analysis: Salvatore Corcione, Vincenzo Cusati and Vittorio Memmolo.
Investigation: Salvatore Corcione, Vincenzo Cusati and Vittorio Memmolo.
Data curation: Salvatore Corcione, Vincenzo Cusati and Vittorio Memmolo.
Writing original draft preparation: Salvatore Corcione, Vincenzo Cusati, Vittorio Memmolo and Fabrizio Nicolosi.
Writing review and editing: Salvatore Corcione, Vincenzo Cusati and Vittorio Memmolo.
Visualization: Salvatore Corcione, Vincenzo Cusati and Vittorio Memmolo.
Supervision: Fabrizio Nicolosi and Raul Llamas Sandin.
Funding acquisition: Fabrizio Nicolosi.

All authors have read and agreed to the published version of the manuscript.

7. Funding

This project has received funding from the European Union's H2020 research and innovation programme under Grant Agreement No. 885052. This publication reflects only the author's view. The European Commission and the CleanSky 2 (Clean Aviation) Joint Undertaking are not responsible for any use that may be made of the information it contains.

Declaration of competing interest

The authors declare the following financial interests/personal relationships which may be considered as potential competing interests: Fabrizio Nicolosi reports financial support was provided by Clean Sky Joint Technology Initiative. Raul Llamas Sandin has patent #US20100148000A1 licensed to Airbus Operations SL.

Data availability

Data will be made available on request.

Appendix A. Insight of an enhanced Vortex Lattice Method

The approach used to achieve a fast and reliable prediction of the aerodynamic loads and lift curve of the tailplane is an improved Vortex Lattice Method (VLM), developed by the research group of the authors [39]. The core methodology is the same as classical vortex methods, such as the one developed by the NASA research centre and published in [48]. Generally speaking, classical vortex methods have some main issues. One issue is their reliability only in the linear range of the lift curve. Additionally, these methods neglect the real airfoil lift coefficient slope and assume a slope equal to 2π (rad^{-1}) based on the Glauert theory. The VLM approach used in this work is based on Blackwell's method [48], but the aerodynamic load distribution is typically obtained using either experimental data or high-fidelity airfoil curves. This approach allows for the extension of aerodynamic results to non-linear lift regions, including the stall.

The method is divided into two main phases. In the first stage, a classic Vortex Lattice Method (VLM) is used to calculate the spanwise lift and induced angle distributions of the wing for a specific angle of attack, denoted by α.

A second stage extends the validity of the VLM approach to the non-linear range of the lift curve by accessing an external database of 2D airfoil aerodynamic curves. To account for the 3D effects, the 2D airfoil data needs to be adjusted. The key aspect to be considered in this respect is the sweep. The sweep produces a boundary layer flow that runs spanwise. Backward sweep promotes stall from the tip, while forward sweep promotes stall from the root. This has been demonstrated in studies conducted by NACA, as reported in the technical note TN-2445 [49].

The 2.5D aerodynamic characteristics of the wing section (perpendicular to the sweep line) are estimated using a basic sweep theory [50] suggests considering the wing section normal to the sweep line, as recommended by Mariens et al. [51]. According to Obert [19], the velocity component perpendicular to the quarter-chord line can be utilized for subsonic wing analysis in practical applications. Because pressure drag acts perpendicular to the isobars [52] (or shock wave line). In case of a transonic wing analysis, the sweep line is considered at the half-chord to position it in close proximity to the shock wave line. This is done to ensure accurate analysis. Additionally, the citation for this information is [52]. [53].

The workflow for estimating the lift coefficient distribution using the enhanced VLM approach is illustrated in Fig. A.19 and it is repeated for each angle of attack. The calculation procedure can be summarized as follows:

1. For each angle of attack, the inviscid lift distribution is calculated through the chosen vortex-lattice approach, by calculating the local C_l at n points along the semispan (typically 50);
2. For all sections, by knowing the local C_l, it is possible to enter the 2D linear lift coefficient chart to obtain the local angle of attack of the airfoil;

$$\left(\alpha_{eff}\right)_j = \left(\alpha_W + \epsilon_j\right) + \left(\alpha_{induced}\right)_j \tag{A.1}$$

3. Using this angle of attack, it is possible to query the airfoil aerodynamic dataset obtaining a new local C_l, which takes into account both viscous and three-dimensional effects;
4. In this way, a new lift distribution along the semi span, which considers the two-dimensional non-linearity, is obtained;
5. This new lift coefficient distribution produces a new distribution of the induced angle of attack, estimated through Prandtl's theory [54].
6. By knowing the new induced angle of attack distribution it is possible to calculate the new angle of attack and lift coefficient distribution.

An iterative process is required from step 2 to step 6. Once convergence is achieved, the lifting surface's C_L can be obtained by integrating the final lift distribution.

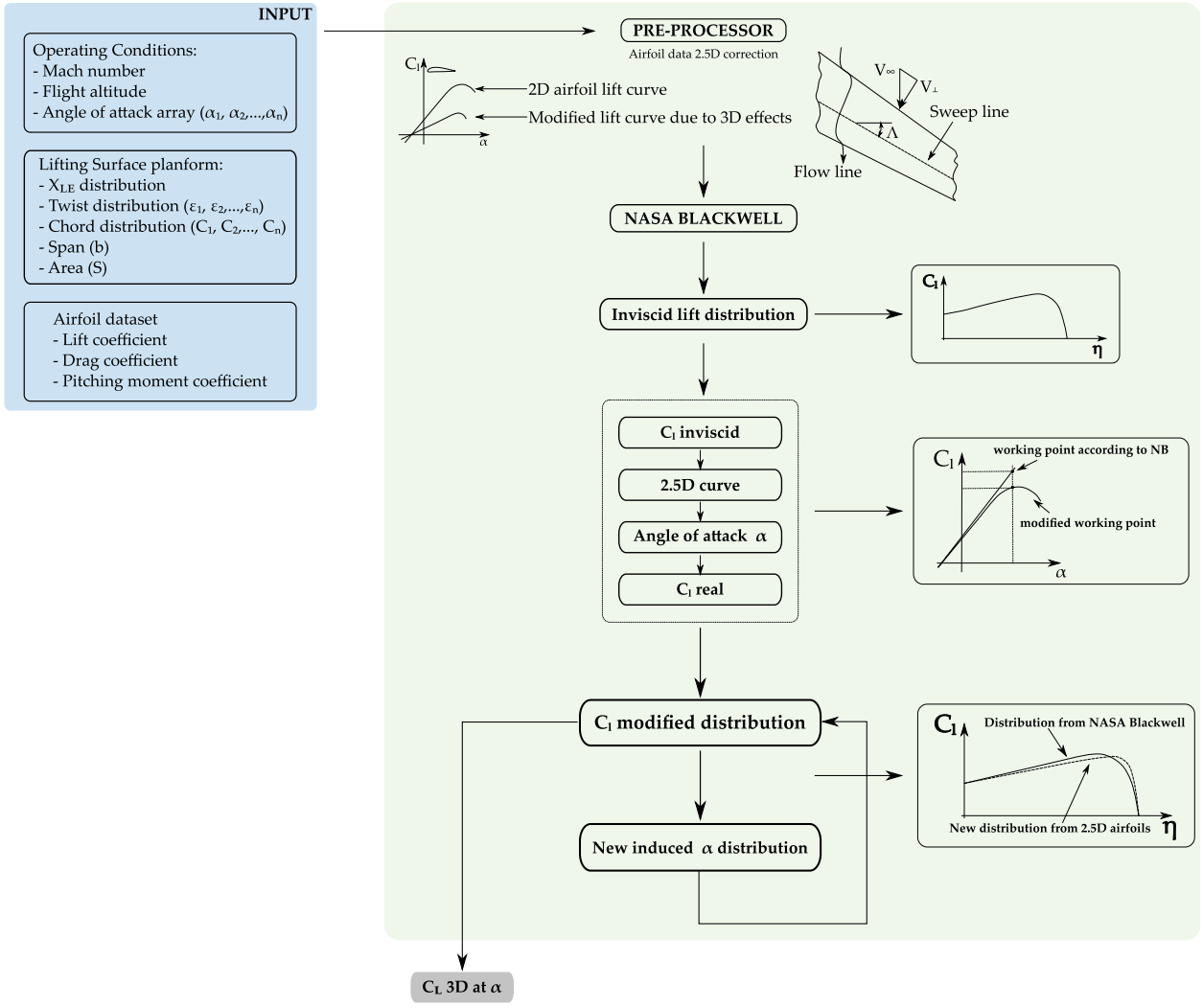

Fig. A.19. Flow chart of lift coefficient distribution through the improved VLM approach.

Appendix B. Insight into structural sizing methodology and deformation analysis

In this section, an overview of the semi-analytical approach used to perform tail structural sizing and deformation analysis is presented.

The functionalities of the tailplane, discussed in section 1, are generated by an aerodynamic force acting on a lever arm, which creates a balancing pitching moment to counteract the pitching moment produced by the combination of the wing and fuselage. The tailplane must ensure longitudinal stability in all operating conditions of an aircraft. To determine the critical loading condition on the tail that drives the structural sizing, the starting point is to construct the classical V-n diagram for the aircraft in question.

According to the aircraft category examined in this paper, the FAR25 regulation [40] can be utilized to establish the flight envelope. An illustration of this diagram is presented in Fig. B.20.

The flight envelope is a diagram useful to define the limit loads for aircraft structures meaning that an aircraft must not fly in a condition laying outside the flight envelope during its operative life. Therefore, the most extreme flight condition is obtained between these limitations. Details and discussions about building up the flight envelope are provided by Calcara and Megson [43,55]. By solving the longitudinal equilibrium equation, it is possible to estimate the necessary aerodynamic load on the tail to balance the aircraft for each flight condition on the V-n diagram. To estimate the most critical loading condition for the tail must be searched among all the steady flight levels and complementary (meaning that the pitching acceleration is not zero) conditions as illustrated by Calcara [43].

The calculation of the flight envelope, in turn, requires some global aircraft data, such as the following:

- $C_{L_{max}}$: maximum lift coefficient
- W_{MTO}: maximum take-off weight
- S_W: wing surface
- ρ_0: density of air at sea level
- n_z: limit load factor
- max forward and backward centre of gravity positions

The critical sizing condition for the tailplane is then translated into a spanwise load distribution, which is used to conduct structural sizing and deformation analysis. Among several methods available to accomplish this task, the Schrenk method [56] has been utilized. To take into account the sweep effect on load distribution Schrenk method has been enhanced by the Pope and Haney correction [57].

The spanwise load can be converted into stress characteristics, which can then be used to size primary structures assuming a cantilever beam.

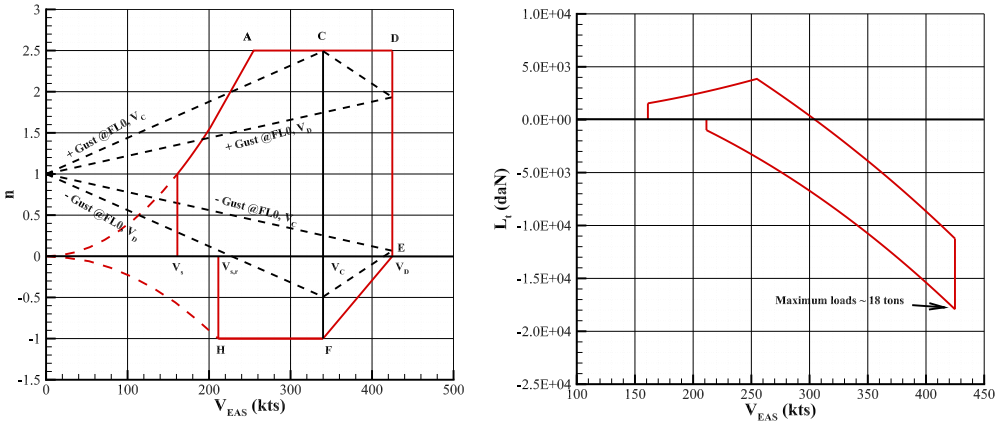

Fig. B.20. Example of a V-n diagram (left) for an A320-like aircraft according to FAR25 [40] and balancing loads on the horizontal tailplane (right).

Generally speaking, the horizontal tail is a 3-D lifting surface that, according to classical aerodynamic theories, can be assumed to be a rigid body whose shape only introduces velocity perturbations in the flow passing over its external surface. A lifting surface is not only a rigid structure but also an elastic body that experiences structural deformation due to the applied load. The elastic behaviour of a lifting surface is typically analyzed using de Saint Venant's (DSV) elementary beam theory [58,59].

According to the DSV theory, the structural sizing of a tailplane modelled as a cantilever beam is affected by:

- N_x: normal stress acting along the beam axis
- S_y, S_z: shear stresses acting along transverse axes
- M_t: torsion moment acting about the beam axis
- M_{b_y}, M_{b_z}: bending moment acting about transverse axes

The low-fidelity model proposed in this work will only consider the S_z, M_b around the longitudinal axis, and M_t as they are the primary stresses affecting the lifting surface deformation. The elastic axis, which represents the locus of the cross-section shear centres, is assumed to be a straight line. This assumption implies that both geometrical and inertial properties are regularly distributed along the span.

Loads acting on the tail structure are due to both aerodynamics and mass distribution. The low-fidelity approach presented here considers the following loads:

- Lift distribution $l_d(y)$: the distribution of force per unit length acting along the vertical axis. The distribution of force depends on the distribution of the span chord, the required lift coefficient, and the dynamic pressure ratio at the sizing conditions. This force distribution is intended to be applied at 25% of the local chord.

$$l_d(y) = \frac{1}{2}\rho V_d^2 c(y) C_{l_d}(y) \tag{B.1}$$

- Aerodynamic pitching torque, denoted as $t_d(y)$, refers to the distribution of torque per unit length about the lateral axis. The dynamic pressure, the square values of the chord distribution along the span ($c(y)^2$), and the pitching moment coefficient about the aerodynamic centre ($C_{m_{ac}}$) are all factors that affect the outcome. This moment is supposed to be applied at the sectional quarter point, as well as for the lift force.

$$t_d(y) = \frac{1}{2}\rho V_d^2 c^2(y) C_{m_{ac}} \tag{B.2}$$

- Weight force $w(y)$ is the distribution of force per unit length displaced along the vertical axis. This depends on the span-wise mass distribution, denoted as m(y), the acceleration due to gravity, denoted as g, and the limit load factor, denoted as n_z:

$$w_d(y) = n_z m(y) g \tag{B.3}$$

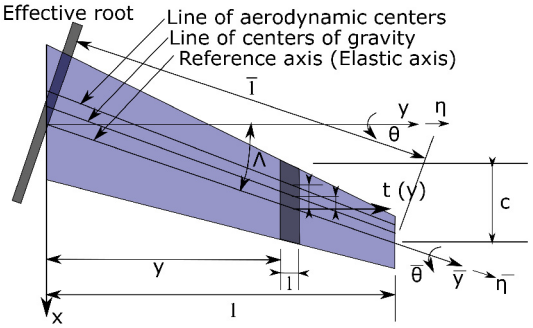

Fig. B.21. Reference coordinate systems for a swept lifting surface.

It is worth highlighting that a triangular distribution is assumed as the initial estimate for the tail mass distribution along the span, based on informed judgement. This distribution is obtained by assuming a statistic value for the total tail mass W_{HT_0}:

$$w_d(y) = -2\frac{n_z W_{HT_0}}{b}\left(1 - \frac{2y}{b}\right) \tag{B.4}$$

Since the analysis focuses on static aeroelastic phenomena, it should be noted that vibratory inertial forces are not considered in the equilibrium equations.

A crucial aspect that needs to be appropriately addressed when evaluating the deformation of a swept lifting surface is the coupling between bending and torsion stresses. In a swept wing, the lateral axis is not aligned with the elastic axis. This requires the introduction of a new axis system by rotating both the x and y axes around the vertical axis by an angle equal to the sweep angle of the elastic axis (Λ_{EA}). In this new reference system, denoted by $\bar{x}\bar{y}$, the lateral axis aligns with the elastic axis, as illustrated in Fig. B.21.

In this new reference frame, the distribution of shear, bending moment, and torsional moment along $\bar{y}$ can be estimated using Eq. (B.5), (B.6), and (B.7), respectively. Here, $\bar{s}$ represents the curvilinear abscissa in the new reference frame.

$$S(\bar{y}) = \int_{\bar{y}}^{\frac{\bar{b}}{2}} [l_d(\bar{s}) + w_d(\bar{s})] d\bar{s} \tag{B.5}$$

$$M_b(\bar{y}) = \int_{\bar{y}}^{\frac{\bar{b}}{2}} S(\bar{s})\, d\bar{s} \tag{B.6}$$

$$M_{t_a}(\bar{y}) = \int_{\bar{y}}^{\frac{\bar{b}}{2}} t_d(\bar{s})\, d\bar{s} \tag{B.7}$$

M_b and M_t are both functions of $\bar{y}$, but from a physical perspective, they are still referred to as moments about the x and y axes, respectively. Therefore, a rotation matrix is required to convert these quantities in moments $\bar{M}_b$ and $\bar{M}_{t_a}$ about $\bar{x}$ and $\bar{y}$ axes. The latter clearly shows that torsion and bending moments are tightly coupled in the case of a swept lifting surface [60], as demonstrated by Eq. (B.8) and Eq. (B.9).

$$\bar{M}_b(\bar{y}) = M_b(y)\cos\Lambda_{EA} - M_{t_a}(y)\sin\Lambda_{EA} \tag{B.8}$$

$$\bar{M}_{t_a}(\bar{y}) = M_b(y)\sin\Lambda_{EA} + M_{t_a}(y)\cos\Lambda_{EA} \tag{B.9}$$

Similar consideration must be done also for the estimate of the level arms of lift and weight forces to take into account for the sweep angle as shown by Eq. (B.10) and Eq. (B.11).

$$\bar{e}_l(\bar{y}) = [x_{ec}(y) - x_{ac}(y)]\cos\Lambda_{EA} \tag{B.10}$$

$$\bar{e}_w(\bar{y}) = [x_{ec}(y) - x_w(y)]\cos\Lambda_{EA} \tag{B.11}$$

Thus, contributions of lift and weight to torsion can be determined using Eq. (B.12) and Eq. (B.13).

$$\bar{M}_{t_l}(y) = \int_{y}^{\frac{\bar{b}}{2}} l_d(\bar{s})\,\bar{e}_l(\bar{s})\, d\bar{s} \tag{B.12}$$

$$\bar{M}_{t_w}(y) = \int_{y}^{\frac{\bar{b}}{2}} w_d(\bar{s})\,\bar{e}_w(\bar{s})\, d\bar{s} \tag{B.13}$$

Finally, the torsional moment is the sum of all contributions as shown by Eq. (B.14).

$$\bar{M}_t(\bar{y}) = \bar{M}_{t_a}(\bar{y}) + \bar{M}_{t_l}(\bar{y}) + \bar{M}_{t_w}(\bar{y}) \tag{B.14}$$

Once the structural loads have been characterized, the sizing of the tailplane structural element can be performed.

The tailplane is modelled as a combination of primary and secondary structures. The mass of the primary structure is calculated using basic structural analysis that relies on stress and deformation measurements. The amount of mass required is only enough to withstand critical loads and/or deformation. Moreover, the computation of the primary structure mass takes into account bending moment relief, material properties, and weight penalties. However, the mass of the secondary structure is estimated statistically, as described in [41]. The tailplane weight model assumes a preliminary division between primary and secondary weight contributions. The primary structure is generally composed of upper and lower stiffened skin panels, spars, ribs, and what is known as the "Non-Optimum Weight," which takes into account weight penalties such as joints, attachments, and cut-outs. The primary structure sustains the main loads applying on the wing. The weight contribution of the previous structure is computed analytically, to the extent possible, based on optimal sizing. The weight contribution of the latter is estimated empirically. The secondary structure is composed of fixed leading and trailing edges, control surfaces, and high-lift devices. The weight of these components is estimated using statistical methods that depend on their geometry. As described above, the problem of tail mass can be expressed as the sum of primary and secondary structure masses.

The primary structure consists of several components. When the lifting surface is under stress, all of its components bear the loads, but some of them are designed to perform specific tasks. A simplified solution for this problem assumes that the wing box is a statically determined equivalent system, where each component bears a specific type of load:

- The caps of the spars are sized to withstand the bending moment (M_b)
- The web of the front and back spars sustains the vertical shear forces (S)
- The covering skin of the wing bears the torsion moment (M_t)
- The ribs support the tail panels against buckling and serve for maintaining the external shape.

Complex structural phenomena, such as the effects of combined loads and dynamic forces, are neglected. Distortion of the cross-section is not considered; flat sections will remain flat after the application of a load.

B.1. Spar caps

Spar is made of web and cap. The two spars may have different heights, in the sizing method, a unique average height h_m, see Eq. (B.15) is assumed and it is obtained by a weighted average through a coefficient α_b being the contribution of one spar to the overall absorption.

$$h_m = h_1\, c(y)\,\alpha_b + h_2\, c(y)\,(1 - \alpha_b) \tag{B.15}$$

The value of α_b can be determined empirically or assessed through the optimization method presented in Section B.6.

The spar cap must absorb the stress (σ) induced by the increase in bending moment (M_b), which is multiplied by the assumed safety margin (S_M). The overall spar cap area, denoted as A_{cap}, must be able to withstand a uniform distribution of stress, represented by σ_y. The resulting sigma distribution is a force that, when multiplied by the lever arm h_m, produces the bending moment M_b. Therefore, the area of the unknown spar caps can be determined using Eq. (B.16).

$$A_{cap}(y) = \frac{S_M\, M_b(y)}{\sigma_y\, h_m(y)} \tag{B.16}$$

The estimated value of A_{cap} may result in impractical thickness values. Indeed, a technological limit t_{lim} is fixed for the ultimate admissible. This means that if the thickness is found to be lower than t_{lim}, it will be replaced with the minimum allowable value.

By knowing the distribution of the area of the spar caps and the material properties, such as the material density (ρ_{mat}), it is possible to estimate the mass of the cap using Eq. (B.17), where g represents the gravitational acceleration. Useful parameters for estimating the distribution of the wing box moment of inertia include the cap thickness, see Eq. (B.18) and the cap span, see Eq. (B.19).

$$w_{cap}(y) = g\, A_{cap}(y)\, \rho_{mat} \tag{B.17}$$

$$t_{cap}(y) = \frac{\sqrt{A_{cap}(y)}}{2} \tag{B.18}$$

$$b_{cap}(y) = 4\, t_{cap}(y) \tag{B.19}$$

B.2. Spar webs

At the conceptual-preliminary design stage, the spar webs are designed to withstand only the vertical shear stresses caused by the aerodynamic and inertial loads. According to the maximum admissible stress approach, the stress on the webs should be lower than both the static (maximum load factor) and fatigue (with $n_z = 1$) rupture stress. Specifically, the spar webs are sized using the method of von Mises considering only the shear stress.

The spar web is assumed to be a rectangle with a height equal to h_m and an unknown area A_{web}. As in the spar web case, A_{web} can be found as that area showing a uniform τ_y, magnified by the safety margin, in absorbing the assigned shear load S.

$$A_{web}(y) = \frac{S_M\, S(y)}{\tau_y} \tag{B.20}$$

By knowing the spar web area also its mass can be estimated by means of Eq. (B.21).

$$w_{web}(y) = g\, A_{web}(y)\, \rho_{mat} \tag{B.21}$$

B.3. Wing box skin

The box's skin must withstand the torque induced by torsion. The wing-box can be modelled as a closed, thin section that reacts to torsion according to Bredt's theory. The area of the box can be calculated using Eq. (B.22) by assuming the chord extension of the wing box is c_{box}.

$$A_{box} = c_{box}\, c(y)\, [h_1(y) + h_2(y)] \tag{B.22}$$

Through the box area, the thickness distribution can be estimated through the first Bredt's theorem that links the thickness and torsion solicitation em as shown in Eq. (B.23).

$$t_{skin} = \frac{1}{2}\, \frac{M_t(y)}{\tau_y\, A_{box}(y)} \tag{B.23}$$

In this case, a technological limit has been imposed on the minimum allowable value for skin thickness. Once the skin thickness is known, the area of the panel skin can be estimated using Eq. (B.24). This, in turn, allows for an estimate of the skin mass using Eq. (B.25).

$$A_{skin} = 2\, c_{box}\, c(y)\, t_{skin}(y) \tag{B.24}$$

$$w_{skin}(y) = g\, A_{skin}(y)\, \rho_{mat} \tag{B.25}$$

To estimate the deformation of the wing box, in addition to material properties, the moment of inertia I is required. The latter depends on the size of the box elements and is given by the sum of the moment of inertia of both the spar and skin, as shown Eq. (B.26) and Eq. (B.27).

$$I_{spar}(y) = \frac{b_{cap}(y)\, h_m(y)^3}{12} - \frac{b_{cap}(y) - 2\left[\frac{A_{web}(y)}{h_m(y)}\right][h_m(y) - 2\, t_{cap}(y)]^3}{12} \tag{B.26}$$

$$I_{skin}(y) = \frac{c_{box}\, c(y)\, h_m(y)^3}{12} - \frac{c_{box}\, c(y)\, [h_m(y) - 2\, t_{skin}(y)]^3}{12} \tag{B.27}$$

B.4. Ribs

The calculation of the mass of the ribs also requires detailed information on the design of the lifting surface. Therefore, a rational approach cannot be used to determine the mass contribution of the ribs. The model assumes that all ribs have the same thickness, which is the minimum required to avoid instability. However, the geometrical pitch varies slightly along the wingspan, and the ribs are only mounted in the working chamber.

The wings are m as panels with an area equal to that of the box, and their thickness and spacing are specified as input data for the wing box layout. Spacing refers to the total number of ribs, denoted as N_{rib}, along the span. Thus, the rib volume V_{rib_i} can be obtained through the Eq. (B.28). The rib mass can be obtained by multiplying the rib volume by the density of the material assumed for the rib, as shown in Eq. (B.28) and (B.29).

$$V_{rib_i} = A_{box_i}\, t_{rib} \tag{B.28}$$

$$M_{rib_i} = A_{box_i}\, t_{rib},\, \rho_{rib} \tag{B.29}$$

B.5. Non-optimum weight

The primary structural elements of the wing box have been fully characterized and will be sized based on critical loads, a safety margin, and the full spectrum of lifting surface operating conditions. However, the actual structure of a lifting surface is not solely composed of primary structural elements.

To determine the weight distribution along the span, there are certain missing elements that are categorized as "non-optimal components" weight in this paper:

- Mountings and connections.
- Aeroelastic corrections.
- Penalties due to the loads and stiffness requirements.
- Thickness variations, joints and large cut-out.

Estimating the mass correction in an analytical manner is not a trivial task. A practical solution to this problem is to consider a certain percentage of the total mass. However, this method should be used with caution since the result may not be consistent with the actual value. Thus, it was decided that the best empirical procedure for estimating the non-optimal weight is Torenbeek's method [41].

B.6. Deformation check

A final design verification is conducted to evaluate the accuracy of the established model. All of the individual components that make up the primary structure are sized according to a specific structural design that is optimized to achieve the lowest possible weight.

In particular, decoupling the load among the spars is the most critical aspect in achieving the optimal balance between stiffness and weight. In detail, the airfoil section can be idealized as a simply supported beam with supports located at the positions of the spars.

Such an equivalent and statically determined system allows to estimate the reaction forces at the front and rear supports (R_F and R_R) according to the specific section load.

To achieve an optimized structure, the front and rear spars should withstand a load ratio that is expressed by Eq. (B.30) and Eq. (B.31).

$$L_F = \frac{R_F\, L}{(R_F + R_R)} \tag{B.30}$$

$$L_R = \frac{R_R\, L}{\left(R_F + R_R\right)} \tag{B.31}$$

Where L represents the total load applied to the chord section, L_F denotes the load supported by the front spar, and L_R represents the load borne by the rear spar. At the conceptual-preliminary design level, this approach is well-suited for defining a more efficient and simplified structural layout.

According to that configuration, the bending and torsional stiffness are computed for every section of the wing. In particular, the torsional stiffness can be divided into two components, primarily related to pure torsion stiffness (as per Bredt's theory) and torsion bending stiffness (as per non-linear theory based on root boundary conditions), as shown in Eq. (B.32).

$$J = J_t + J_b \tag{B.32}$$

Finally, these stiffness properties are utilized to discretize a beam-like model, where the stiffness of the shoes is equivalent to that of the wing-box. The rotation and deformation of each section are then checked to account for wing flexibility and to assess whether it exceeds critical values.

B.7. Wing box deformation

The lifting surface has been modelled as a wing box that must withstand only S, M_b, and M_t. Moreover, the distribution of shear strain is neglected because its effects are considered to be of second order.

By knowing the distributions of bending and torsion stiffness, it is possible to calculate the two main types of deformation:

- v: displacements along Z axis
- θ: rotations around beam axis

Those two cinematic variables are the key structural deformations in this study because they represent the displacements provided by the most severe loads acting on the tail.

These variables are calculated for points laying on the beam axis representing, in this perspective, the lifting surface itself. Thus, a simplifying assumption is made that the cross-section shape does not cause any distortion of the camber line. This means that the section airfoil aerodynamics does not change because of the lifting surface deformation: the effect is on the three-dimensional surface.

The elastic deformation about the beam axis interpreted by torsion is responsible for the distortions of the aerodynamic loads distribution (i.e. torsion modifies the local geometric twist along the span affecting local angles of attack).

The resulting J is employed to obtain θ as a function of the beam axis coordinate, that is y for a straight wing in the way the reference system has been fixed. The relation between the first derivative of the torsion angle arises from the equilibrium of the beam element under the action of M_t, as shown in Eq. (B.33). Whereas the bending moment introduces vertical displacements given by the Euler-Bernoulli relation shown in Eq. (B.34), $I(y) = I_{spar(y)} + I_{skin}(y)$.

$$\frac{\partial\theta}{\partial y} = -\frac{M_t(y)}{G\, J(y)} \tag{B.33}$$

$$\frac{\partial^2 z}{\partial y^2} = \frac{M_b(y)}{E\, I(y)} \tag{B.34}$$

Sweep introduces a strong connection between bending and torsion. This coupling also reflects its impact on the point of view of cinematic variables. Thus, there is a need to consider the various angles in both the streamwise and chordwise directions. Because of the rotation of the beam axis with respect to y axis, in the case of a swept lifting surface, the relation is the one shown by Eq. (B.35).

$$\frac{\partial\bar{\theta}}{\partial\bar{y}} = -\frac{\bar{M}_t(\bar{y})}{G\, J(\bar{y})} \tag{B.35}$$

In the case of a swept lifting surface, rotations occur about the $\bar{y}$ axis. However, an additional angle must be added to the flow incidence angle to evaluate the aerodynamic load distortion caused by elastic deformations. It is important to note that the incidence angle is measured with respect to the y axis. Thus, twist angles must be converted into the initial reference system using Eq. (B.36).

$$\theta(y) = \bar{\theta}(\bar{y})\cos\Lambda_{EC} - \frac{\partial z}{\partial\bar{y}}\sin\Lambda_{EC} \tag{B.36}$$

B.8. Secondary structure

The secondary structure is composed of fixed leading and trailing edges, control surfaces, and high-lift devices. The weight of these components is estimated using statistical methods that depend on their geometry. The aim here is to estimate the mass of the secondary structure in order to complete the computation of the lifting surface mass.

The secondary mass typically contributes approximately 30% of the total wing mass and has a significant impact on inertial relief.

Due to the complexity of the various components, a statistical approach seems useful in estimating the contribution of secondary mass.

Two main methods are being considered. The first approach, based on Roux's assumptions, seems to be plausible [61]. It has been suggested that the mass of the secondary structure is proportional to the power of the lifting surface reference area of the wing. This approach appears to be reliable because it allows for remarkable precision in relation to the set of surface mass data. Following this approach, we have Eq. (B.37).

$$M_{secondary} = 0.488\ \mathrm{K}\ S_{ref}^{n} \tag{B.37}$$

Where:

- K = 25.9 and n = 1.097 if $W_{MTO} > 10000$ N.
- K = 4.39 and n = 1.358 if $W_{MTO} < 10000$ N.

The problem with this approach is that it neglects to consider the configuration of secondary structural components. Such a misleading assumption can lead to an inaccurate result if that configuration is already known. That is the reason why Torenbeek's work is significant. According to Torenbeek's semi-empirical equations, the estimation of the secondary mass contribution can be accurately determined if all necessary details are provided [41]. The approach enables us to obtain a formal solution for each category, including high-lift devices, control surfaces, and others. This is achieved by utilizing statistical data and functional parameters, such as the type of flaps, various device surfaces, and the maximum takeoff weight (W_{MTO}). For these reasons, it was decided to implement Torenbeek's method when the required design data is available and to use a purely statistical approach when no data is available.

References

[1] R. Martinez-Val, E. Perez, Aeronautics and astronautics: recent progress and future trends, Proc. Inst. Mech. Eng., Part C, J. Mech. Eng. Sci. 223 (2009) 2767–2820, https://doi.org/10.1243/09544062JMES1546.
[2] R. Liebeck, Design of the blendedwing body subsonic transport, J. Aircr. 41 (2004) 10–25, https://doi.org/10.2514/1.9084.

[3] L. Zhoujie, R. Martins, Aerodynamic design optimization studies of a blended-wing-body aircraft, J. Aircr. 51 (2014) 1604–1617, https://doi.org/10.2514/1.C032491.
[4] M. Picchi Scardaoni, M. Montemurro, E. Panettieri, Prandtlplane wing-box least-weight design: a multi-scale optimisation approach, Aerosp. Sci. Technol. 106 (2020) 106–156, https://doi.org/10.1016/j.ast.2020.106156.
[5] A. Tasca, V. Cipolla, K. Salem, M. Puccini, Innovative box-wing aircraft: emissions and climate change, Sustainability 223 (2009) 2767–2820, https://doi.org/10.1243/09544062JMES1546.
[6] J. Garcia-Benitez, C. Cuerno-Rejado, R. Gomez-Blanco, Conceptual design of a nonplanar wing airliner, Aircr. Eng. Aerosp. Technol. 88 (2016) 561–571, https://doi.org/10.1108/AEAT-11-2014-0204.
[7] S. Pandaya, External aerodynamics simulations for the mit d8 “double-bubble” aircraft design, in: 7th International Conference on Computational Fluid Dynamics (ICCFD7), 2012.
[8] B. Yutko, N. Titchener, T. Chambers, C. Courtin, M. Lieu, T. Roberts, J. Tylko, L. Wirsing, Nonlinear static aeroelastic and trim analysis of highly flexible joined-wing aircraft, in: 17th AIAA Aviation Technology, Integration, and Operations Conference, 2017, pp. 1–36.
[9] J. Anderson, Aircraft Performance and Design, WCB McGraw-Hill, Boston, MA, USA, 1999.
[10] A. Sánchez-Carmona, C. Cuerno-Rejado, L. García-Hernández, Unconventional tail configurations for transport aircraft, in: Progress in Flight Physics, vol. 9, 2017, pp. 127–148.
[11] A. Sánchez-Carmona, C. Cuerno-Rejado, Vee-tail conceptual design criteria for commercial transport aeroplanes, Chin. J. Aeronaut. 32 (3) (2019) 595–610, https://doi.org/10.1016/j.cja.2018.06.012.
[12] CleanSky, New empennage for aircraft (nefa), https://cordis.europa.eu/project/id/G4RD-CT-2002-00864.
[13] J. Frota, K. Nicholls, M. Müller, P. Gall, J. Loerke, K. Macgregor, P. Schmollgruber, J. Russell, M. Hepperle, S. Dron, K. Plötner, G. Gallant, Final activity report. New aircraft concept research (nacre), nACRE Consortium, Blagnac, France, 2010.
[14] R. Llamas Sandin, M. Luque Buzo, Aircraft horizontal stabilizer surface, US 2010/0148000 A1, 2010, https://patents.google.com/patent/US20100148000A1/en.
[15] A. Seitz, M. Kruse, T. Wunderlich, J. Bold, L. Heinrich, The dlr project lamair: design of a nlf forward swept wing for short and medium range transport application, in: 29th AIAA Applied Aerodynamics Conference, 2012.
[16] A. Seitz, A. Hübner, K. Risse, The dlr tulam project: design of a short and medium range transport aircraft with forward swept nlf wing, CEAS Aeronaut. J. (2020), https://doi.org/10.1007/s13272-019-00421-1.
[17] J. Roskam, C. Lan, Airplane Aerodynamics and Performance, DARcorporation, Lawrence, Kansas 66044, USA, 1997.
[18] J. Bertin, R. Cummings, Aerodynamics for Engineers, Pearson Education International, Upper Saddle River, NJ, 2009.
[19] E. Obert, Aerodynamic Design of Transport Aircraft, IOS Press, Netherlands, 2009.
[20] R. Skoog, H. Brown, Method for the determination of the spanwise distribution of a flexible swept wing at subsonic speed, Tech. Rep. NACA TN2222, National Advisory Committee for Aeronautics, Washington, USA, 1951, https://ntrs.nasa.gov/citations/19930082867.
[21] R. Skoog, An analysis of the effects of aeroelasticity on static longitudinal stability and control of a swept-wing airplane, Tech. Rep. NACA-TR-1298, National Advisory Committee for Aeronautics, Washington, USA, 1957, https://ntrs.nasa.gov/citations/19930092293.
[22] S. Gemma, F. Mastroddi, Multi-disciplinary and multi-objective optimization of an over-wing-nacelle aircraft concept, CEAS Aeronaut. J. 10 (2018) 771–793, https://doi.org/10.1007/s13272-018-0347-7.
[23] M. Biancolini, C. Groth, S. Porziani, A. Chiappa, F. Giorgetti, F. Nicolosi, U. Cella, Validation of structural modeling for realistic wing topologies involved in fsi analyses: ribes test case, J. Aerosp. Eng. 34 (1) (2021) 04020110, https://doi.org/10.1061/(ASCE)AS.1943-5525.0001200, https://ascelibrary.org/doi/pdf/10.1061/%28ASCE%29AS.1943-5525.0001200.
[24] C. Groth, M. Biancolini, E. Costa, U. Cella, Validation of high fidelity computational methods for aeronautical fsi analyses, in: M. Biancolini, U. Cella (Eds.), Flexible Engineering Toward Green Aircraft, in: Lecture Notes in Applied and Computational Mechanics, vol. 92, Springer International Publishing, 2020, pp. 29–48.
[25] Z. Lyu, J. Martins, Aerodynamic design optimization studies of a blended-wing-body aircraft, J. Aircr. 51 (5) (2014) 1604–1617, https://doi.org/10.2514/1.C032491.
[26] Z. Lyu, K. Kenway, J. Martins, Aerodynamic shape optimization studies on the common research model wing bench-mark, AIAA J. 53 (4) (2014) 968–985, https://doi.org/10.2514/1.J053318.
[27] G. Kenway, J. Martins, Multipoint high-fidelity aerostructural optimization of a transport aircraft configuration, J. Aircr. 51 (1) (2014) 1604–1617, https://doi.org/10.2514/1.C032150.
[28] J. Jasa, J. Hwang, J. Martins, Open-source coupled aerostructural optimization using Python, Struct. Multidiscip. Optim. 57 (2018) 1815–1827, https://doi.org/10.1007/s00158-018-1912-8.
[29] S. Chauhan, J. Martins, Low-fidelity aerostructural optimization of aircraft wings with a simplified wingbox model using openaerostruct, in: International Conference on Engineering Optimization, 2018, pp. 418–431.
[30] T.R. Brooks, G. Kenway, J. Martins, Undeflected common research model (ucrm): an aerostructural model for the study of high aspect ratio transport aircraft wings, in: 35th AIAA Applied Aerodynamics Conference, 2017.
[31] A. Elham, M. van Tooren, Coupled adjoint aerostructural wing optimization, using quasi-three-dimensional aerodynamic analysis, Struct. Multidiscip. Optim. 54 (2017) 889–906, https://doi.org/10.1007/s00158-016-1447-9.
[32] X. Changchuan, A. Chao, Y. Liu, Y. Chao, Static aeroelastic analysis including geometric nonlinearities based on reduced order model, Chin. J. Aeronaut. 30 (2) (2017) 638–650, https://doi.org/10.1016/j.cja.2016.12.031.
[33] X. Changchuan, M. Yang, W. Fei, W. Zhiqiang, Aeroelastic optimization design for high-aspect-ratio wings with large deformation, Shock Vib. 2017 (2017) (2017) 1–16, https://doi.org/10.1155/2017/2564314.
[34] D. Scholz, Empennage sizing with the tail volume complemented with a method for dorsal fin layout, INCAS Bull. 13 (3) (2021) 149–164, https://doi.org/10.13111/2066-8201.2021.13.3.13.
[35] J. Roskam, Methods for Estimating Stability and Control Derivatives of Conventional Subsonic Airplanes, Roskam Aviation and Engineering Corporation, Lawrence, Kansas, USA, 1971.
[36] W. Philips, Mechanics of Flight, 2nd edition, John Wiley & Sons, Inc., Hoboken, New Jersey, USA, 2009.
[37] D. Raymer, American Institute of Aeronautics and Astronautics, American Institute of Aeronautics and Astronautics, Washington, D.C., USA, 2013.
[38] P. Albuquerque, F. Cunha, L. Reis, Evaluation of structural loads, https://doi.org/10.13140/2.1.4615.3288, 2012.
[39] P. Della Vecchia, F. Nicolosi, M. Ruocco, L. Stingo, A. De Marco, An improved high-lift aerodynamic prediction method for transport aircraft, CEAS Aeronaut. J. (2019) 795–804, https://doi.org/10.1007/s13272-018-0349-5.
[40] F.A. Administration, Far part 25 – airworthiness standards: normal category airplanes, https://www.ecfr.gov/current/title-14/part-25.
[41] E. Torenbeek, Synthesis of Subsonic Airplane Design: An Introduction to the Preliminary Design, of Subsonic General Aviation and Transport Aircraft, with Emphasis on Layout, Aerodynamic Design, Propulsion, and Performance, Delft University Press, 1982.
[42] IMPACT, Impact EU project website, https://www.impact-cleansky-project.eu/.
[43] M. Calcara, Elementi di dinamica del veivolo, CUEN, 1988.
[44] Software Siemens PLM, Simcenter STAR-CCM+ software, https://www.plm.automation.siemens.com/global/it/products/simcenter/, 2017.
[45] F. Nicolosi, A. De Marco, L. Attanasio, P. Della Vecchia, Development of a Java-based framework for aircraft preliminary design and optimization, J. Aerosp. Inform. Syst. 13 (2016) 1–9, https://doi.org/10.2514/1.I010404.
[46] A. De Marco, V. Trifari, F. Nicolosi, M. Ruocco, A simulation-based performance analysis tool for aircraft design workflows, Aerospace 7 (11) (2020), https://doi.org/10.3390/aerospace7110155, https://www.mdpi.com/2226-4310/7/11/155.
[47] CleanSky, Clean sky’s advanced rear end demo shapes up, https://www.clean-aviation.eu/media/results-stories/clean-skys-advanced-rear-end-demo-shapes-up.
[48] J.J. Blackwell, A finite-step method for calculation of theoretical load distributions for arbitrary lifting-surface arrangements at subsonic speeds, Tech. Rep. NASA TN D-5335, National Aeronautics and Space Administration, Washington, USA, 1969, https://ntrs.nasa.gov/citations/19690021959.
[49] P. Purser, M. Spearman, Wind-tunnel tests at low speed of swept and yawed wings having various plan forms, Tech. Rep. NACA TN-2445, National Advisory Committee for Aeronautics, Washington, USA, 1951, https://ntrs.nasa.gov/citations/19930083063.
[50] D.R. Holt, Introduction to transonic aerodynamics of aerofoils and wings, Tech. Rep. ESDU Data Item 90008, ESDU, London, U.K., 1990, https://www.esdu.com/cgi-bin/ps.pl?sess=unlicensed_1220304093323cgp&t=doc&p=esdu_90008#.
[51] J. Mariens, A. Elham, M. van Tooren, Quasi-three-dimensional aerodynamic solver for multidisciplinary design optimization of lifting surfaces, J. Aircr. 51 (2) (2014) 547–558, https://doi.org/10.2514/1.C032261.
[52] I. Desktop, Aeronautics, oblique flying wings: an introduction and white paper, https://www.desktop.aero/library/ofwwhitepaper.pdf, 2005.
[53] M. Drela, Simultaneous Optimization of the Airframe, Powerplant, and Operation of Transport Aircraft, Hamilton Place, London, 2010.
[54] J.D. Anderson, Fundamentals of Aerodynamics, McGraw Hill, Boston, MA, USA, 2007.
[55] T. Megson, Aircraft Structures for Engineering Students, 6th edition, Butterworth-Heinemann, 2016.
[56] O. Schrenk, A simple approximation method for obtaining the spanwise lift distribution, Tech. Rep. NACA-TM-948, National Advisory for Aeronautics, Washington, D.C., USA, 1940, https://ntrs.nasa.gov/citations/19930094469.
[57] A. Pope, W.J. Haney, Readers forum, J. Aeronaut. Sci. 16 (8) (1949) 505–511, https://doi.org/10.2514/8.11841.
[58] A. de Saint Venant, Mémoire sur la torsion des prismes, avec des considérations sur leur flexion ainsi que sur l’équilibre intérieur des solides élastiques en général, et des formules pratiques pour le calcul de leur résistance à divers efforts s’exercant simultanément, 14, 1856, pp. 233–560, Mémoires Présentés par divers savants à l’Académie des sciences de l’Institut de France.

[59] A. de Saint Venant, Mémoire sur la flexion des prismes, sur les glissements transversaux et longitudinaux qui l'accompagnent lorsqu'elle ne s'opère pas uniformément ou en arc de cercle, et sur la forme courbe affectée alors par leurs sections transversales primitivement planes, J. Math. Pures Appl. 2 (1) (1856) 88–189, http://eudml.org/doc/234512.

[60] T. Lomax, Structural Loads Analysis for Commercial Transport Aircraft Theory and Practice, AAIA, 2013.

[61] E. Roux, Modèle de masse voilure avions de transport civil pour une approche analytique de la dynamique du vol, http://elodieroux.com/EditionsElodieRouxBonus_Reports.html.